Is Anthropogenic Global Warming Accelerating?

STUART JENKINS,[a] ADAM POVEY,[b] ANDREW GETTELMAN,[c] ROY GRAINGER,[b] PHILIP STIER,[a] AND MYLES ALLEN[a,d]

[a] *Atmospheric, Oceanic and Planetary Physics, Department of Physics, University of Oxford, Oxford, United Kingdom*
[b] *National Centre for Earth Observation, Department of Physics, University of Oxford, Oxford, United Kingdom*
[c] *National Center for Atmospheric Research, Boulder, Colorado*
[d] *Environmental Change Institute, School of Geography, University of Oxford, Oxford, United Kingdom*

(Manuscript received 7 February 2022, in final form 19 June 2022)

ABSTRACT: Estimates of the anthropogenic effective radiative forcing (ERF) trend have increased by 50% since 2000 (from +0.4 W m^{-2} $decade^{-1}$ in 2000–09 to +0.6 W m^{-2} $decade^{-1}$ in 2010–19), the majority of which is driven by changes in the aerosol ERF trend, as a result of aerosol emissions reductions. Here we study the extent to which observations of the climate system agree with these ERF assumptions. We use a large ERF ensemble from the IPCC's Sixth Assessment Report (AR6) to attribute the anthropogenic contributions to global mean surface temperature (GMST), top-of-atmosphere radiative flux, and we use aerosol optical depth observations. The GMST trend has increased from +0.18°C $decade^{-1}$ in 2000–09 to +0.35°C $decade^{-1}$ in 2010–19, coinciding with the anthropogenic warming trend rising from +0.19°C $decade^{-1}$ in 2000–09 to +0.24°C $decade^{-1}$ in 2010–19. This, as well as observed trends in top-of-atmosphere radiative fluxes and aerosol optical depths, supports the claim of an aerosol-induced temporary acceleration in the rate of warming. However, all three observation datasets additionally suggest that smaller aerosol ERF trend changes are compatible with observations since 2000, since radiative flux and GMST trends are significantly influenced by internal variability over this period. A *zero-trend-change* aerosol ERF scenario results in a much smaller anthropogenic warming acceleration since 2000 but is poorly represented in AR6's ERF ensemble. Short-term ERF trends are difficult to verify using observations, so caution is required in predictions or policy judgments that depend on them, such as estimates of current anthropogenic warming trend, and the time remaining to, or the outstanding carbon budget consistent with, 1.5°C warming. Further systematic research focused on quantifying trends and early identification of acceleration or deceleration is required.

KEYWORDS: Aerosols; Radiative fluxes; Radiative forcing; Temperature; Trends

1. Introduction

The anthropogenic contribution to global warming was around 1.1° ± 0.2°C above preindustrial levels between 2000 and 2019 and rising at +0.2°C $decade^{-1}$ (Allen et al. 2018; Gillett et al. 2021; WMO 2019). Over the same period the globally averaged effective radiative forcing (ERF) (Myhre et al. 2013; Forster et al. 2016), which drives the anthropogenic contribution to warming, has monotonically increased by approximately +0.4 W m^{-2} $decade^{-1}$, with the 2000–20 mean anthropogenic RF reaching ~2.1 W m^{-2} (1.3–3.0 W m^{-2}) above preindustrial levels (Myhre et al. 2013; Forster et al. 2021).

The relationship between global radiative forcing changes and the global surface temperature anomaly response is captured with a linearized forcing-feedback framework:

$$\Delta F = \Delta N + \lambda \Delta T, \tag{1}$$

where an ERF perturbation ΔF is equated to the sum of a perturbation in the top-of-atmosphere (TOA) radiative flux ΔN, which, through the small heat capacity of the atmosphere, equates with the rate of heat uptake by the oceans and cryosphere, and a linear feedback proportional to the globally averaged surface temperature ($\lambda \Delta T$). The use of ERF in Eq. (1) means that rapid feedbacks (subannual time scale responses in atmospheric composition, temperature profile, etc.) are accounted for in the definition of the forcing. Given an estimate of the ERF change over an interval ΔF and an estimate of the net global feedback parameter λ, Eq. (1) describes the response of the global temperature and TOA flux anomaly. Equivalently, Eq. (1) can be used with observations of the climate system to estimate the time history of ERF [e.g., see Dong et al. (2021), in which a linear energy balance framework is used to deconstruct a TOA flux anomaly into forced and feedback contributions in CMIP6 models].

Leading up to the IPCC's Sixth Assessment Report a number of studies produced revised estimates of the ERF contributions from individual forcing agents, which are used in attributions of the level and rate of anthropogenic warming (Dessler and Forster 2018; Smith et al. 2021a). Several ERF datasets now suggest that net anthropogenic ERF has accelerated since 2000,

Denotes content that is immediately available upon publication as open access.

Supplemental information related to this paper is available at the Journals Online website: https://doi.org/10.1175/JCLI-D-22-0081.s1.

Corresponding author: Stuart Jenkins, stuart.jenkins@wadham.ox.ac.uk

DOI: 10.1175/JCLI-D-22-0081.1

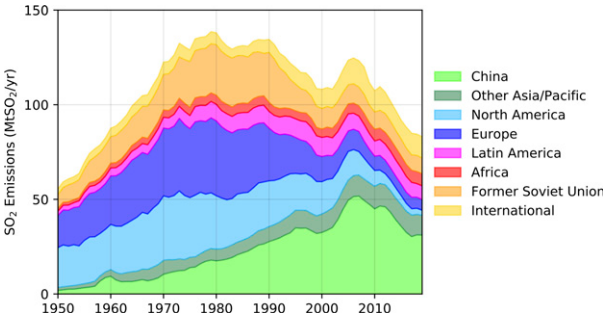

FIG. 1. CEDS SO_2 emissions inventory showing global SO_2 emissions since 1960 (McDuffie et al. 2020). SO_2 emissions are colored by region, such that global emissions are the sum of all stacked regions. The international emissions category includes global shipping and aircraft emissions, since these are not aligned with any single territory.

principally because of declining anthropogenic aerosol emissions since the early 2000s (McDuffie et al. 2020) and rising emissions of major GHGs (CO_2, CH_4, and N_2O) (NOAA 2021a). Figure 1 shows anthropogenic SO_2 emissions from the Community Emissions Data System (CEDS) database, a major contribution to aerosol ERF, colored by region according to broad regional denominations in the CEDS (McDuffie et al. 2020). SO_2 emissions have declined by around a third since peaking in 2005, and simultaneously have shifted geographically from the Northern Hemisphere midlatitudes to predominantly be emitted in Southeast Asia. These aerosol emissions estimates have a large and almost immediate impact on aerosol ERF trends.

However, care must be taken in attributing an acceleration in human-induced global warming to these changes in aerosol emissions. Short-term global mean surface temperature (GMST) variability is strongly influenced by internal variability processes and other factors unrelated to anthropogenic forcing (e.g., the relative ENSO and PDO state, variability in sea surface temperatures and the rate of ocean heat uptake, and volcanic eruptions), meaning the underlying anthropogenic ERF trend changes can be obscured over short observational records. Even if the impact of internal variability were well understood and could be accounted for over the historical record, there remain uncertainties in the ERF time series used for an attribution procedure, due to upstream uncertainties in anthropogenic emissions accounting and because of uncertainties in the climate system's response to individual forcing agents. This problem is particularly prominent for aerosol ERF estimates (Forster et al. 2021), where quantifying the magnitude of aerosol–cloud interactions over the historical record remains challenging (Bellouin et al. 2020).

Since the 1990s the near-global coverage of Earth-observing satellites has enhanced direct measurement of several indicators of global energy imbalance, including near-surface air temperatures (NASA Goddard Institute for Space Studies 2018; Morice et al. 2021; Smith et al. 2008), TOA radiative fluxes (Loeb et al. 2017; Poulsen et al. 2020), and atmospheric concentrations of GHGs and aerosols (Sogacheva et al. 2020; NOAA 2021a). Alongside this, climate models provide an ensemble of historical simulations (Eyring et al. 2016; Pincus et al. 2016), which have been used to constrain individual pollutant's ERFs by decomposing model-derived GMST responses into externally forced behavior, feedbacks, and natural variability (Flynn and Mauritsen 2020). Such approaches have been used to estimate the anthropogenic contribution to global warming (Gillett et al. 2021), and to assess the sensitivity of the climate system to future anthropogenic perturbations (Donohoe et al. 2014; Murphy et al. 2009; Sherwood et al. 2020; Dessler and Forster 2018; Zelinka et al. 2020).

Several groups identify a linear trend in TOA flux and GMST datasets and go on to estimate the contribution of these trends from anthropogenic ERF between 2000 and 2020. Kramer et al. (2021) use radiative kernels to deconstruct CERES TOA fluxes (Loeb et al. 2017) into forced contributions and temperature-mediated feedbacks, identifying a 20-yr linear trend in net TOA flux that they attribute to the linear trend in greenhouse gas ERF (Kramer et al. 2021). Similarly, Raghuraman et al. (2021) identify a statistically significant linear trend in the net TOA flux that cannot be explained by internal variability alone, but is explained once anthropogenic forcing is included.

These studies provide direct observational evidence of a linear trend in anthropogenic ERF, largely attributed to greenhouse gas emissions over the period since 2000. Isolating an aerosol contribution to these trends is more challenging. Kramer et al. (2021) find the SW TOA flux record is largely controlled by temperature-mediated feedbacks and changes in cloud cover [similar to results discussed in Loeb et al. (2019)]. Loeb et al. (2021) use a partial radiative perturbation decomposition of the observed TOA flux anomalies to determine that aerosol forcing has contributed very little to the overall trend in Earth's energy imbalance over the past two decades, with much more from cloud cover variability and temperature-mediated feedbacks (Loeb et al. 2021). However, none of these studies consider the possibility that the rate of anthropogenic warming has changed since 2000, despite the suggestion in ERF datasets that the anthropogenic ERF trend has not remained constant over the period.

Here, we analyze the direct observational evidence of an acceleration in ERF between 2000 and 2020. In section 2, we explore individual pollutants' contributions to global ERF trends in standard ERF datasets, demonstrating that aerosols are the principal driver of the perceived acceleration in ERF since 2000. In section 3, these ERF trend assumptions are tested against three observational datasets that have near-global coverage over the last two decades: 1) the GMST anomaly, 2) the TOA radiative flux anomaly, and 3) aerosol optical depth (AOD) observations. Section 4 concludes and discusses options to generate an ERF ensemble that reflects recent observations of the global climate system.

2. Near-present ERF estimates

We use the best-estimate historical ERF time series from the Shared Socioeconomic Pathways (SSPs) ERFs (Smith 2020): a series of standardized mitigation scenarios with various

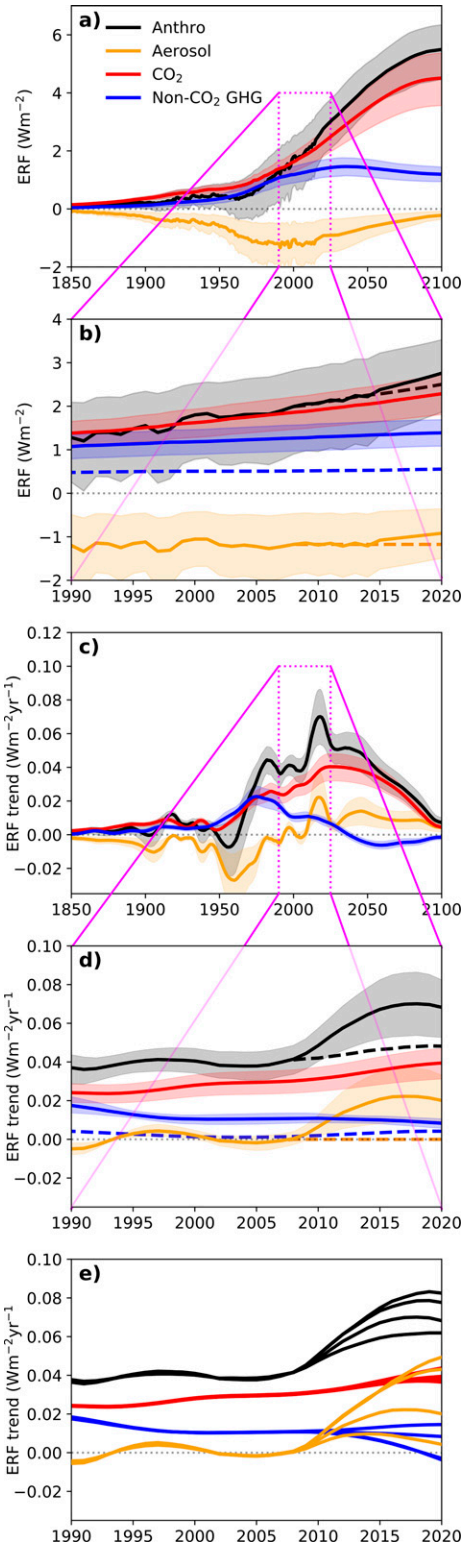

FIG. 2. Globally averaged effective radiative forcing (ERF) time series from Smith et al. (2021a). (a) Contributions from CO_2 (red), non-CO_2 GHGs and other minor contributors (blue), and aerosols (orange) to the total anthropogenic ERF time series (black). (c) Contributions of each component to the total ERF trend, estimated with a triangularly weighted mean over 10-yr linear gradients estimated with OLS regression. Best-estimate ERF is plotted with a solid line, and shading shows the 5th–95th-percentile range. Historical ERF estimates run to December 2014; ERF is extended to 2100 using SSP2-45. Also shown are (b),(d) zoomed-in versions of (a) and (c), respectively, highlighting the period 1990–2020. (e) Best-estimate trends of other SSP variants (SSP1-19, SSP1-26, SSP2-45, and SSP3-70). Dashed blue lines in (b) and (d) show the methane ERF level and trend in isolation. On the same panels, orange dashed lines show an alternative aerosol ERF scenario in which the ERF trend remains zero after 2010. Black dashed lines show the corresponding anthropogenic ERF for this aerosol ERF scenario.

assumptions of climate policy ambition, along with separate realizations of twenty-first-century development (global cooperation, technological innovation, and population change). SSP scenarios feature heavily in research into the response of the climate system to anthropogenic emissions over the twenty-first century (IPCC 2018; Eyring et al. 2016; Pincus et al. 2016; Collins et al. 2017).

In Fig. 2 the *historical*+SSP2-45 net anthropogenic ERF time series (Smith 2020) is plotted (black), along with contributions from CO_2 (red), other well-mixed GHGs and minor contributors (blue), and aerosols (orange). The ERF time series are estimated from global emissions and concentration time series using adapted simple formulas as described in Forster et al. (2021) for GHGs and Smith et al. (2021a) for aerosols, based on a harmonization between CMIP6 ERF estimates (Pincus et al. 2016; Collins et al. 2017) and observational constraints (Smith et al. 2021a). A description of the production methodology is provided in the online supplemental material, and further information can be found in the supplementary material to chapter 7 of IPCC's AR6 (Smith et al. 2021b). Figure 2a plots the individual ERF component time series between 1850 and 2100, relative to a preindustrial baseline set in 1750. SSP2-45 is used beyond 2015 to approximate a "current policies" future trajectory, as this approximately represents current ambition for CO_2 and other GHG emissions (SSP2-45 is also used to extend many historical experiments to 2100 in CMIP6 DECK simulations; Pincus et al. 2016). The SSP2-45, SSP1-26, and SSP1-19 variants show similar reductions in aerosol emissions between 2015 and 2020, which approximately match the CEDS emissions time series in Fig. 1, whereas SSP3-70 delays mitigation until later in the twenty-first century (Rao et al. 2017). Figure 2c shows corresponding ERF trends for each component of ERF plotted in Fig. 2a, where the trend is calculated using a triangularly weighted mean of rolling 10-yr ordinary least squares (OLS) linear regressions on the time series in Fig. 2a. Alternative trend estimation methodologies yield similar results (see the online supplemental material). Figures 2b and 2d highlight the period 1990–2020 where near-global and near-continuous observational records exist. In the context of decadal global trends, we argue that the data beyond 2020 are anomalous due to the impact of COVID (the impact of COVID has been explored elsewhere; e.g., Le Quéré et al. 2020).

The 5th–95th-percentile uncertainty range of each ERF component is shown with shading around the median ERF time series. Fractional uncertainty in each ERF component covers the 2019 likely range reported in IPCC's AR6 for GHG components (Forster et al. 2021) and in Smith et al. (2021a) for present-decade aerosol uncertainty. Anthropogenic ERF is calculated by summing independently sampled ERF components (assuming no correlation between individual forcing agents) to produce a 1000-member ERF ensemble, following the approach described in Dessler and Forster (2018). This methodology correlates the uncertainty in ERF levels (Fig. 2b) and trends (Fig. 2d), since the present-day uncertainty is sampled by rescaling a single best-estimate ERF shape over history. Consequently, extremes in a pollutant's present-day ERF level only arise for time series that also exhibit extreme trends over the near-present period, potentially undersampling the range of plausible ERF trends.

Figure 2b shows that the majority of the historical ERF comes from CO_2, a well-mixed GHG for which we have a long observational record (NOAA 2021a; Friedlingstein et al. 2020). The contribution from non-CO_2 GHGs in Fig. 2b is smaller, and over much of history approximately offsets a negative aerosol ERF. Most of the warming signal at the present day is attributed to CO_2, but this could change rapidly in the future if non-CO_2 GHG forcing persists while aerosol forcing declines. This scenario is often overlooked in idealized mitigation scenarios, where mitigation takes place uniformly over many pollutants simultaneously, but may already be happening as nations put particulate emissions controls in place (Zhang et al. 2019) with less clear action on CO_2 and other non-CO_2 pollutants. Aerosol ERF remains the most uncertain contribution to overall anthropogenic ERF (5th–95th-percentile range covering between -0.5 and -1.8 W m^{-2} in Fig. 2), with smaller contributions from aerosol–radiation interactions than aerosol–cloud interactions (Zelinka et al. 2020; Bellouin et al. 2020). Trends in individual ERF components have received relatively little research attention to date, potentially because of continued challenges in assessing the ERF level, with observational records only recently becoming mature enough to offer insights.

Anthropogenic ERF has accelerated since 2000 (from $+0.4$ W m^{-2} decade^{-1} in 2000–09 to $+0.6$ W m^{-2} decade^{-1} in 2010–19; black line in Fig. 2d). The acceleration is present in the full 5th–95th-percentile range plotted, meaning that SSP2-45's ERF ensemble assumes the rate at which humans are contributing to global warming is increasing. The extent of this acceleration is shown in black in Fig. 3 over the two decades 2000–20. SSP2-45's trend is around $+0.25$ W m^{-2} decade^{-1} higher in the second decade (2010–19) than in the first decade (2000–09)—a substantial increase relative to historical anthropogenic ERF trends. Further, the driver for this trend increase is unusual in comparison with the historical drivers of ERF trends. In the twentieth century the predominant cause of an increasing anthropogenic ERF trend has been the rise in annual CO_2 emissions. Figure 2 suggests that since 2000 the predominant cause of the acceleration is aerosols, driven by a peak and decline in the (negative) aerosol ERF (see the aerosol ERF shape in Fig. 2a). Methane ERF contributes little to the anthropogenic ERF behavior (the dashed blue line in Figs. 2b and 2d depicts the methane ERF contribution), rising from $+0.49$ to $+0.54$ W m^{-2} between 2000 and 2020 (Smith et al. 2021b). Recent revisions to the global carbon budget (Friedlingstein et al. 2022) also suggest that CO_2 emissions have been stable, not increasing, since 2010, meaning that the CO_2-induced ERF trend is approximately constant since 2010 as well. SSP2-45's $+0.19$ W m^{-2} decade^{-1} increase in aerosol ERF trend between 2000–09 and 2010–19 accounts for the majority of the anthropogenic ERF trend change in Fig. 2.

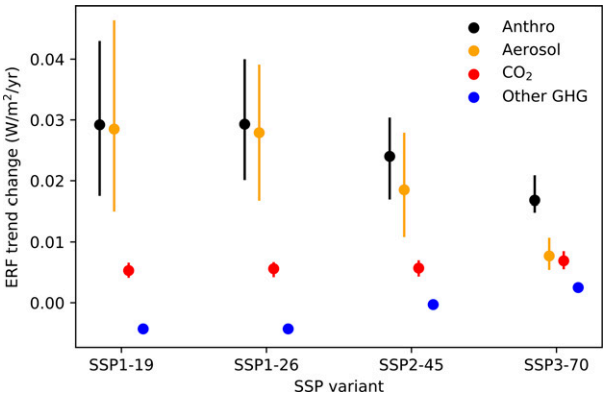

FIG. 3. The ERF decadal trend change is driven by aerosol trends. Shown is the trend change between 2000–10 and 2010–20 in each SSP variant that was plotted in Fig. 2e. The decadal trend changes between 2000 and 2020 are calculated using the average gradient in each decade, as calculated in Fig. 2d, with each component's gradient change shown for each SSP variant (red = CO_2; blue = non-CO_2 GHGs; orange = aerosols; black = total).

The accelerating anthropogenic ERF is not a unique feature of the SSP2-45 scenario. SSP1-26 and SSP1-19 suggest that aerosols are the cause of anthropogenic ERF acceleration since 2000, while SSP3-70 (with delayed aerosol mitigation) has a smaller trend change. Figures 2e and 3 show how the choice of SSP variant beyond 2014 changes the relative size of the anthropogenic ERF trend change, and the contribution from aerosols to this trend change. The aerosol ERF trend covers a range from $+0.05$ to $+0.45$ W m^{-2} decade^{-1} in 2020 depending on how ambitious the chosen scenario is after 2014, despite all the scenarios' trends being identical and near-zero in 2010. In SSP1-19 (a 1.5°C-compatible mitigation scenario) there is a much greater aerosol ERF trend change than in the less ambitious SSP2-45 scenario ($+0.29$ W m^{-2} decade^{-1}, as compared with $+0.19$ W m^{-2} decade^{-1}). This is expected given the higher-ambition policy that SSP1-19 represents, achieving net-zero CO_2 emissions around 2050 along with rapid aerosol and non-CO_2 GHG emissions reductions.

3. Observations as a constraint on aerosol forcing assumptions

Justification for the shapes of Fig. 2's ERFs is usually provided using emissions datasets. Figure 1 shows the SO_2 emissions according to the CEDS dataset (a major component of total anthropogenic aerosol emissions; Stevens 2015), which

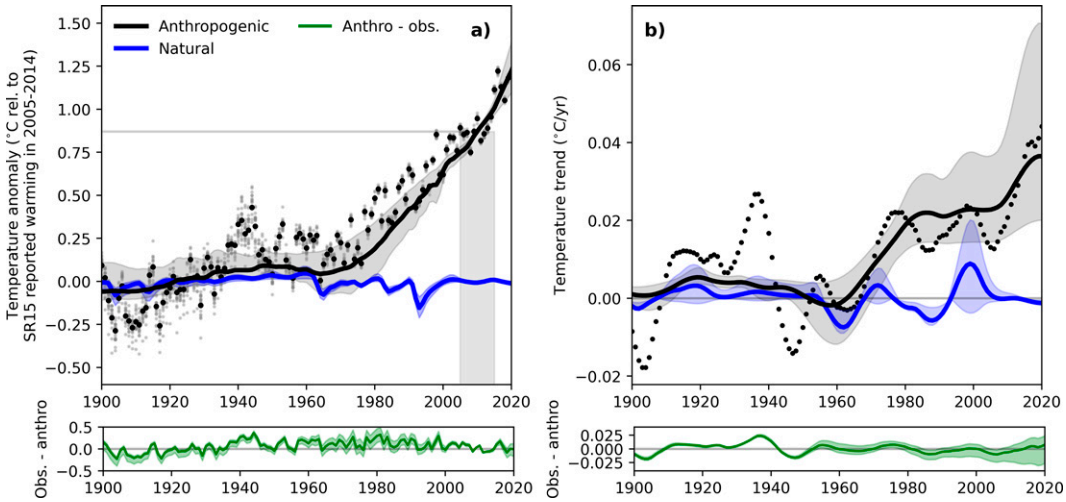

FIG. 4. The level and rate of anthropogenic warming between 1900 and 2020: (a) results using the methodology of Haustein et al. (2017) along with radiative forcing estimates from Fig. 2 to estimate the level of anthropogenic warming (black) in comparison with natural forcing (blue), and (b) the corresponding trend for each contribution to the global temperature anomaly. Shading shows the 5th–95th-percentile uncertainty range. Observed temperatures from a four-dataset mean are plotted as black points (with individual ensemble uncertainty shown in gray); the level of warming is baselined to the SR1.5 reported warming over the period 2006–15 inclusive [gray region in (a)]. Green lines below each panel show the difference between the observed monthly temperature anomaly and anthropogenic temperature anomaly.

are estimated to have peaked around 2005, while CO_2, CH_4, and N_2O concentrations have remained stable or increased since 2000. After 2015, reported GHG and aerosol emissions are best represented by the SSP2-45 scenario's emissions time series (Rao et al. 2017; Meinshausen et al. 2020) leading to the ERF time series shown in Fig. 2. Aerosol ERF trends become positive after 2010, leading to the substantial change in the overall anthropogenic ERF trend.

But what if the ERF trends in Fig. 2 are wrong? While global anthropogenic aerosol emissions are reported to be in decline since 2005 as a result of emissions reductions in Southeast Asia, the spatial pattern of aerosol emissions has also redistributed toward the tropics from the Northern Hemisphere midlatitudes over this period. This redistribution may influence cloud properties over the tropical Pacific (Kasoar et al. 2018), with some research suggesting a greater response for aerosol ERF perturbations over the Southeast Asian region when compared with similar perturbations over other Northern Hemisphere midlatitude regions (Shindell et al. 2012), which may offset the ERF change expected following a reduction in anthropogenic aerosol emissions. A further concern is the impact of reporting biases and estimation errors in bottom-up emissions estimates, such as those produced by CEDS, biasing ERF estimates produced with these global emissions time series. Southeast Asian sulfate emissions may have been substantially underreported over the late twentieth century, whereas since 2000 the surface dimming/brightening trends in the region are remarkably stable in comparison with corresponding emissions estimates (Moseid et al. 2020).

Hence, there is reason to be cautious of Fig. 2's proposed ERF trend changes since 2000. To explore which ERF trends are representative of observed changes in the Earth system over the last two decades, below we use global surface temperature anomalies, TOA radiative flux anomalies, and AODs to derive observational constraints on the recent ERF trend change, focusing on the attribution of the aerosol contribution since 2000. Because the climate system is already in disequilibrium in 2000, downstream observables will be influenced both by variations in our present-day inputs (i.e., aerosol loading, GHG concentrations, internal variability) and by the pre-2000 perturbation's influence on unforced variability. We compare the observed climate system's response since 2000 with modeled responses using the SSP2-45 ERF scenario shown in Fig. 2, and other scenarios with alternative aerosol ERF assumptions: SSP3-70, and a variant of SSP2-45 in which no aerosol ERF trend change occurs (the "no aerosol trend change" scenario shown with dashed orange and black lines on Fig. 2). A full discussion of the datasets and analysis methodologies used can be found below in section 3a.

a. Datasets and methods

1) GMST DATASETS AND ATTRIBUTION METHODOLOGY

Figures 4 and 5 show two attributions of various anthropogenic and natural ERF contributions to the GMST anomaly. We define the global mean surface temperature using an average over several GMST products, following the approach of the IPCC's Special Report on Global Warming of 1.5°C (Allen et al. 2018; SR1.5). We consider four in situ datasets that use statistical infilling to produce near-global coverage:

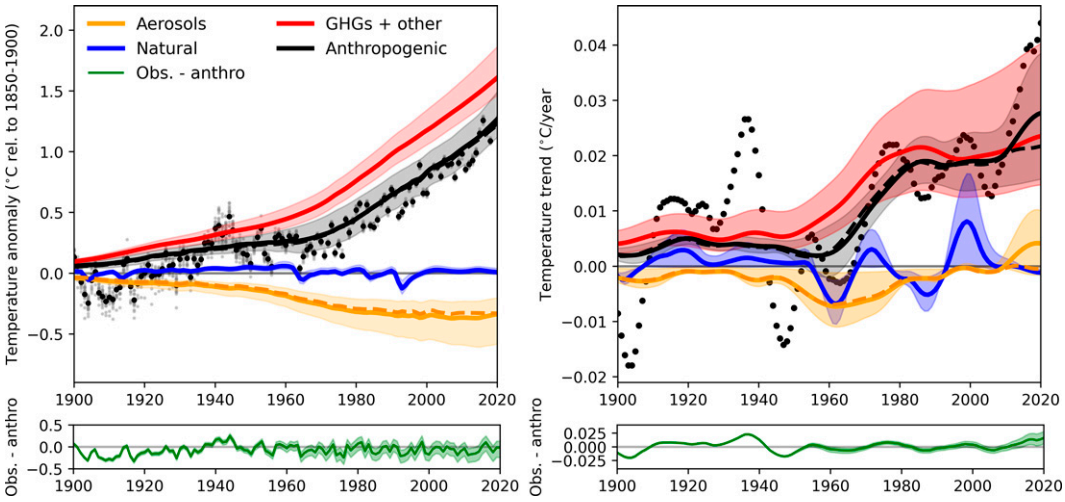

FIG. 5. A three-way attribution of aerosols, greenhouse gases, and natural ERF contributions onto GMST observations, showing the level and rate of anthropogenic warming between 1900 and 2020: (left) the level of human-induced warming using the methodology of Haustein et al. (2017), and (right) the warming trend for each contribution. Observed temperatures from a four-dataset mean are plotted in black (with individual ensemble uncertainty shown in gray). In both panels, the orange line corresponds to the attributed aerosol contribution to global temperatures; blue shows the natural contribution and red shows the GHG contribution; black shows the total anthropogenic contribution. Shading shows the 5th–95th-percentile uncertainty range. Green lines below each panel show the difference between attributed anthropogenic warming and the observed GMST anomaly. Orange and black dashed lines show the alternative attribution result if the dashed *zero-trend* aerosol ERF scenario from Fig. 2 is used in the attribution instead.

HadCRUT5 (Morice et al. 2021), NOAA (Smith et al. 2008), BerkeleyEarth (Rohde and Hausfather 2020), and GISTEMP (NASA Goddard Institute for Space Studies 2018). Although this means that datasets produced with different infilling approaches, data coverage and time periods are mixed, it is unlikely this will significantly skew results since differences between these datasets are much smaller than the assumed uncertainty within any single dataset (Allen et al. 2018).

To study the ERF–temperature response relationship using observations we use the procedures laid out in Hasselmann (1997) and Hegerl et al. (1996), where possible contributions to an observable are attributed using OLS regression and detection of a contributing signal is confirmed if the significance of the fingerprinted pattern is found above a given threshold (e.g., 95%). Here we do this by following the related Haustein et al. (2017) methodology, which uses characteristic temperature response shapes to fingerprint contributions to globally averaged GMST (Haustein et al. 2017). The Finite Amplitude Impulse Response model (FaIRv2.0; Leach et al. 2021) derives an ensemble of globally averaged temperature responses using SSP2-45's anthropogenic and natural ERF time series from Fig. 2 as input. The temperature responses are derived using 20 response parameter configurations in FaIR to sample the full range of physical response behaviors, meaning each natural and anthropogenic forcing pair corresponds to 20 temperature response pairs. A three-layer temperature-box setup is used in FaIR, as Tsutsui (2020) finds this gives a better fit to short-time-scale forced variability in the climate system under abrupt forcing changes, although results would be very similar with a two-box setup as in earlier versions of FaIR (Smith et al. 2018; Millar et al. 2017). The derived temperature response pairs are regressed onto the GMST anomaly, additionally sampling observational uncertainty (200-member ensemble; Morice et al. 2021) and natural variability (102-member ensemble CMIP6 PIControl runs; Eyring et al. 2016) in the GMST time series. In total each forcing pair produces around 400 000 temperature response pairs, which are then sampled to find the median and 5th–95th-percentile-range temperature response attributable to the natural and anthropogenic ERFs.

2) TOA FLUX ANOMALY DATASETS AND TREND ANALYSIS

The TOA flux anomalies in Fig. 6 are calculated by removing the average seasonal cycle over the record, defined as the mean monthly TOA flux value. The left column contains observed TOA fluxes from the CERES EBAF4.1 record (Loeb et al. 2017), the middle column has prescribed-SST atmosphere-only simulations with the CESM2 model (Gettelman et al. 2019) forced with *historical*+SSP3-70 concentrations and emissions precursors, and the right column has an ensemble of coupled atmosphere–ocean simulations forced with *historical*+SSP2-45 concentrations and emissions precursors, following the Radiative Forcing Model Intercomparison Project (RFMIP) hist-all protocol (Pincus et al. 2016). All the panels assume that a positive TOA flux anomaly is oriented radially outward from Earth's surface, corresponding to radiative cooling, and thus negative anomalies correspond to warming. Across all panels we fit blue trend lines to the flux anomalies to estimate

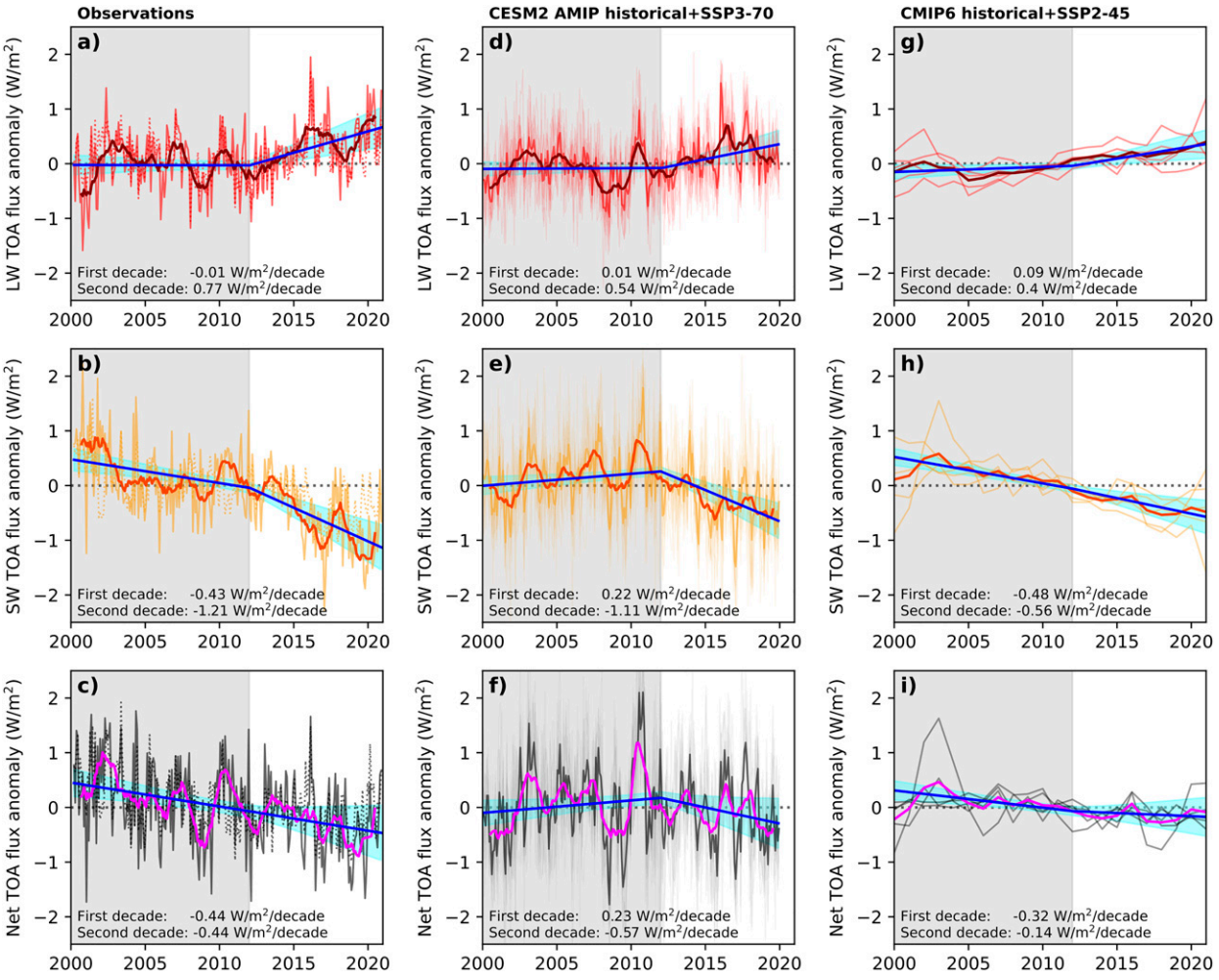

FIG. 6. Comparing radiative flux anomalies in observations and GCMs: (a)–(c) TOA radiative flux anomalies from the CERES EBAFv4.1 satellite observations product, (d)–(f) a 10-member ensemble of CESM2 AMIP runs with externally imposed SSTs, and (g)–(i) the ensemble mean TOA flux anomaly from five CMIP6 models, showing (top) the LW flux anomaly (red), (middle) the SW flux anomaly (orange), and (bottom) the net flux anomaly (black). Twelve-month running means are shown with a thick line over each time series, along with a decadal trend (blue shading). GLS regression estimates the decadal linear trends, assuming an AR(1) process in the residuals. Resulting decadal trend estimates are noted in the bottom left of each panel. CMIP6 TOA flux anomalies in (g)–(i) are found using a multimodel mean over individual TOA flux anomalies in *historical*+SSP2-45 experiments. Years 2000–12 are shaded with gray to denote the "pause in global warming" period.

the decadal linear trends using a generalized least squares regression. This fit uses a fixed breakpoint piecewise linear regression, with the breakpoint in 2012, considered the end of the pause in global warming period (IPCC et al. 2013), and assumes autocorrelated residuals using an AR(1) process. A detailed description of the fitting procedure for the blue trend lines is in the online supplemental material.

To estimate feedback parameter values, we complete a regression of the GMST anomaly onto the full time series of net TOA flux anomalies [adjusted with the ensemble of anthropogenic ERFs from Fig. 2 along with an additional stratospheric aerosol RF time series from the Global Space-based Stratospheric Aerosol Climatology (GloSSACv2; Kovilakam et al. 2020)]. We bootstrap the regression to estimate the uncertainty following Dessler and Forster's (2018) approach (subsampling the 20-yr TOA flux anomaly record with replacement to account for correlation between consecutive data points).

For the coupled atmosphere–ocean model experiments the LW, SW, and net TOA flux anomaly are calculated using runs of the *historical*+SSP2-45 experiment with five CMIP6 models for which we have corresponding ERF time series from RFMIP (CanESM5, HadGEM3-GC31-LL, IPSL-CM6A-LR, GISS-E2-1-G, and NorESM2-LM); the multimodel-mean flux anomaly is shown with a thick line in each panel, with individual models shown with thin lines. The *historical*+SSP2-45 experiment uses a coupled atmosphere–ocean setup, meaning the natural variability over the 20-yr period is randomized for each model run. Plotting the ensemble average over each model (as is shown in the right-hand column's panels) averages out the impact of historical unforced SST and cloud cover

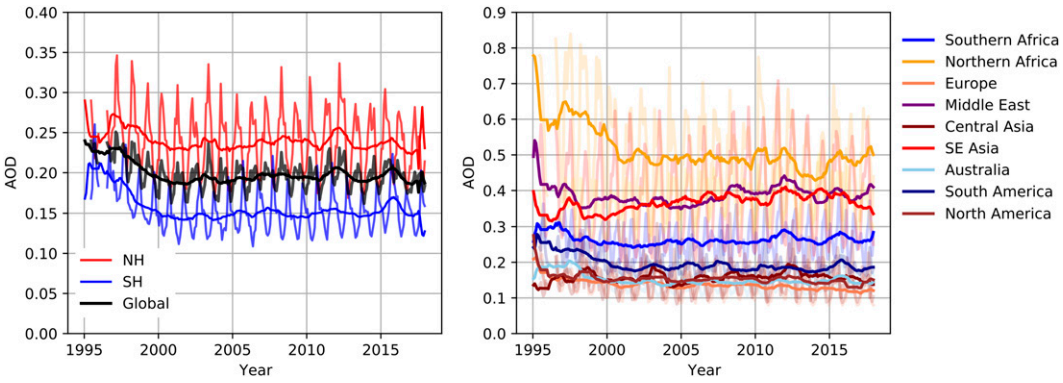

FIG. 7. Aerosol optical depth time series plotted from Sogacheva et al. (2020) between 1995 and 2018: (left) global and hemispheric averages and (right) AOD time series of several broad geographical regions. In each panel, monthly anomalies are shown with their seasonal cycles, with thick lines superimposed that plot the annual anomaly (12-month rolling mean). In the left panel, the red line plots the Northern Hemispheric average, the blue line plots the Southern Hemispheric average, and a global average is shown in black. In the right panel, key geographical regions include Southeast Asia (red), the Middle East (purple), and northern Africa (yellow).

variability, isolating the model's response to external forcing changes. LW, SW, and net feedbacks for these five CMIP6 models [found using each model's flux anomaly, global surface temperature anomaly, and ERF time series from the transient ERF experiment in RFMIP (Pincus et al. 2016)] are consistent with the estimates made using the 4 × CO_2 experiment (see Fig. S6 in the online supplemental material).

For the atmosphere-only simulations *historical* runs are completed using the CESM2 GCM (Gettelman et al. 2019). Here, SST and sea ice coverage from reanalysis products (Huang et al. 2017; Rayner et al. 2003) drive the CAM6 atmospheric model between 2000 and 2020, while boundary conditions mimic observed SST variability over the two decades. This means decadal trends in internal variability, forced from SSTs, are also included in the middle column of Fig. 6 (assuming cloud cover natural variability, principally over the tropical Pacific, is largely driven by the SST boundary conditions).

3) AEROSOL OPTICAL DEPTH DATASETS AND TREND ANALYSIS

Aerosol optical depth (AOD) has been measured with satellite-based equipment since around 1980 (Poulsen et al. 2020; NOAA 2021c). Sogacheva et al. (2020) produce an AOD product that combines several of these records to produce a near-global time series between 1995 and 2018. From this synthesized AOD record globally, hemispherically, and regionally averaged anomalies (calculated by removing their mean seasonal cycle over the full record) are plotted in Fig. 7. Regional trends are calculated over broad geographical regions defined in Table S1 and Fig. S6 of the online supplemental material.

We first consider a linear global relationship between SO_2 emissions and the anthropogenic contribution to AOD, since anthropogenic aerosol species have an extremely short atmospheric lifetime, so the annual emissions have an approximate one-to-one correspondence with the annual atmospheric aerosol burden. Using this we can estimate the expected AOD trend change using Fig. 1's SO_2 emissions changes, assuming that SO_2 emissions act as a good proxy for total anthropogenic aerosol emissions (Stevens 2015).

Figure 8's trend estimates rely on a split decadal linear trendline fit using GLS regression onto individual model's AOD and ERF time series, as was done in Fig. 6's decadal trend fit. We use the same five CMIP6 models as in the right column of Fig. 6, for which we have corresponding historical ERF time series to derive a global relationship between changes in AOD trend and corresponding changes in ERF trend. Trends are calculated for the observation time series in the left panel of Fig. 7 and for a subset of CMIP6 models using their historical AOD time series and corresponding ERF time series from RFMIP's transient ERF experiment (Pincus et al. 2016). The CMIP6 model trends are shown in Fig. S7 of the online supplemental material.

b. *The global temperature anomaly*

Figure 4 shows the attributed level (Fig. 4a) and trend (Fig. 4b) of contributions to the observed GMST anomaly. Warming contributions from natural (blue) and anthropogenic (black) ERFs are plotted on top of GMSTs (black scatterpoints). The anthropogenic temperature anomaly tracks the GMST anomaly over the historical record in Fig. 4a—it is clear that anthropogenic influences are responsible for the majority of observed warming to date (Allen et al. 2018). The range of anthropogenic warming in the decade 2010–19 is 1.04°C [0.98°–1.10°C for 5th–95th-percentile range; rebaselined to the IPCC's near-term baseline of 0.85°C in 2006–15 above 1850–900 levels (Allen et al. 2018)]. This aligns with attribution studies used in AR6, which find warming around 1.1°C above 1850–900 over the past decade (Gillett et al. 2021; Haustein et al. 2017; Ribes et al. 2021). Gillett et al. (2021) use a similar regression approach to analyze the anthropogenic contribution to global temperatures, but exchange the FaIR-derived temperature responses for an ensemble of GMST-like concentration-driven temperature responses found by masking surface air temperatures from the historical

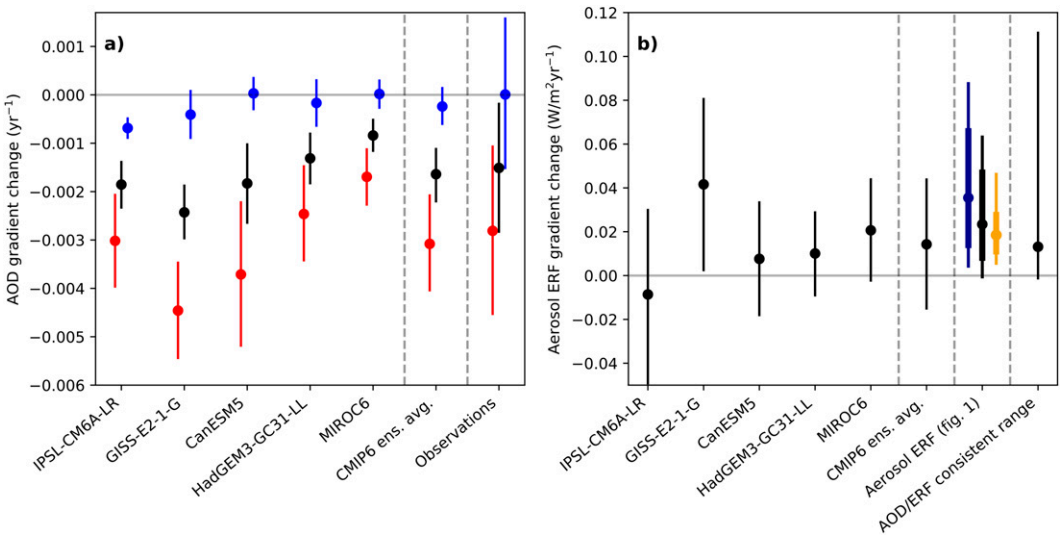

FIG. 8. AOD and ERF gradient changes between 2000 and 2020 for CMIP6 models and satellite observations: (a) the AOD gradient change, including averages over the Northern Hemisphere (red), Southern Hemisphere (blue), and global domains (black), and (b) the ERF trend changes using the RFMIP transient ERF experiment. All trend changes are measured using a linear trend that is split in 2010. This trend is fit using GLS regression onto each time series [assuming an AR(1) process autocorrelates the residual], and the process is identical to that in Fig. 6. In (a), the CMIP6 ensemble mean AOD trend change is shown, alongside the AOD gradient change measured in observations from Fig. 7. In (b) the ensemble mean CMIP6 ERF trend change is shown alongside the assessed gradient change in standard ERF time series from Fig. 2. The standard dataset's aerosol ERF trend change is assessed in three ways: 1) using decadal averages of the trends plotted in Fig. 2d (orange scatterpoint), 2) using GLS regression identical to that used for the CMIP6 models (blue scatterpoint), and 3) using GLS regression and comparing the gradients over an extended historical period (i.e., gradient change between 1990–2010 and 2010–20). The rightmost scatterpoint in (b) shows the implied aerosol ERF trend change, given the observed AOD trend change, calculated using the CMIP6-mean linear relationship between AOD trend changes and the resulting aerosol ERF trend changes.

experiments of CMIP6 models (Gillett et al. 2021). They conclude that the majority of the warming observed in GMST is explained by anthropogenic contributions alone, with anthropogenic warming averaging 1.1°C between 2010 and 2019.

In Fig. 4b the multidecadal trend in GMST observations is broadly reproduced using the anthropogenic ERF ensemble from Fig. 2. Over shorter intervals the GMST anomaly's trend can vary substantially, for example in the early twentieth century with departures of around 0.1°–0.2°C decade^{-1} away from the anthropogenic warming trend in the 1930s and 1940s. These deviations are typically explained as evidence of early Arctic warming or other exceptional events tied to internal variability (Hegerl et al. 2018), along with the impact of reduced regional coverage of observations. Since 2000, the GMST trend (black scatterpoints in Fig. 4b) has again deviated substantially above +0.18°C decade^{-1} (2000–09) to +0.35°C decade^{-1} by 2010–19. Internal variability processes (principally trends in cloudiness and SSTs in the tropical Pacific) provide one possible explanation for these trend changes since 2000 (Loeb et al. 2019), and may, at least in part, arise from the shift from La Niña to strong El Niño between the 2000s and 2010s (see Fig. 9 with a particularly strong El Niño event, with a Ñino-3 index above 2.0, in 2015/16). Other variability signals, such as the PDO (with a negative-to-positive swing over the last two decades, also shown in Fig. 9), could also play a role in explaining recent GMST trends (Masson-Delmotte et al. 2021).

Despite these covarying variability signals, unlike in the early twentieth century the post-2000 warming trend change is largely attributed to anthropogenic forcing changes in Fig. 4b (i.e., the black line tracks the black scatterpoints) because the underlying anthropogenic ERF itself contains a substantial trend change over this period. Hence, Fig. 4b's anthropogenic warming trend rises from +0.21 (+0.13 to +0.35)°C decade^{-1} in 2000–09 to around +0.33 (+0.20 to +0.56)°C decade^{-1} in 2010–19 (brackets show the 5th–95th percentile range); a 65% increase in the best-estimate anthropogenic warming rate.

1) SEPARATING THE AEROSOL AND GHG CONTRIBUTIONS

If the anthropogenic and natural ERFs are a perfect description of the external forcings that result in the observed GMST behavior, then the residual should contain only the internal variability of the climate system. Consider the residual below Fig. 4: while in Fig. 4a the broad characteristics the GMST anomaly behavior are reproduced, the residual remains positive throughout the second half of the twentieth century. This bears the characteristics of strong aerosol forcing also found in some CMIP6 GCMs (e.g., Sellar et al. 2019;

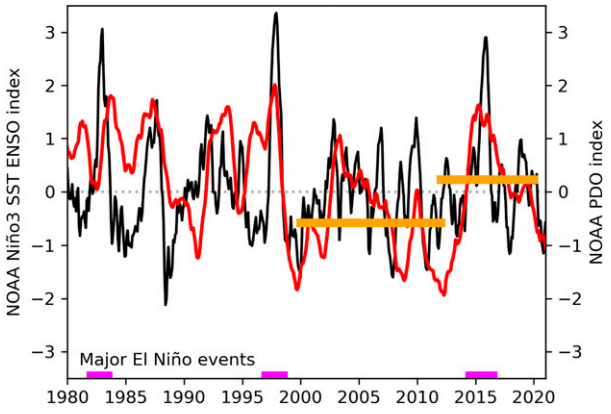

FIG. 9. ENSO variability plays a key role in determining short-term temperature variability. This plot shows a time series of the relative ENSO state over the tropical Pacific Ocean (black) from NOAA's Niño-3 record (NOAA 2021b). Significant positive El Niño events are highlighted with pink regions along the *x* axis (defined as having a Niño-3.0 index above 2.0). The PDO signal (red) tracks significant deviations in the ENSO record and has a lower mean value through the period of "paused" global warming (2000–12; −0.51), than afterward (2012–20; +0.22), as marked with orange bars.

Swart et al. 2019): anthropogenic warming is held artificially low until the mid-twentieth century when aerosol forcing peaks, and then accelerates more rapidly than observed GMST after 1980 as negative aerosol forcing declines, potentially exaggerating the aerosol warming trend contribution since 2000. Alternatively, it is possible that Fig. 4's residual could be explained by a combination of changes in heat uptake, unforced variability, and changes in the net feedback parameter. A change in the net feedback strength, for example due to the changing spatiotemporal pattern of aerosol emissions, could contribute to this residual behavior, and requires further research (Wilcox et al. 2022). However, the other explanations are less plausible; Zanna et al. (2019) do not observe a significant change in the rate of ocean heat uptake between the mid-twentieth century and present day, and since the residual is biased low over several decades consecutively it is unlikely this departure can be explained solely by internal variability.

To study the individual contributions from aerosols and GHGs, the attribution procedure is repeated using a three-way regression, allowing the aerosol warming to be rescaled separately to the GHG and natural warming. The aerosol (orange), GHG (red), anthropogenic (aerosol + GHG; black) and natural (blue) contributions to the warming level (Fig. 4a) and rate (Fig. 4b) are shown in the left panel of Fig. 5. Aerosol cooling lies around −0.35°C (from −0.20° to −0.65°C) between 2010 and 2019, relative to 1850–1900. GHG warming is 1.50°C (1.35°–1.70°C) over 2010–19, meaning anthropogenic warming overall is 1.09°C (1.00°–1.30°C) in 2010–19, consistent with other recent attribution studies (Gillett et al. 2021; Masson-Delmotte et al. 2021; Forster et al. 2021).

Based on the fit to GMST observations, the left panel of Fig. 5 offers a better explanation of the twentieth-century contributions from aerosols, GHGs, and natural ERFs to global warming. The aerosol warming contribution is scaled down substantially (the best-estimate aerosol scaling factor is around 0.62; see Fig. S2 in the online supplemental material), while the GHG warming contribution is kept closer to its assumed value in Fig. 4 (the GHG scaling factor is 0.90). Downscaling the aerosol contribution reduces the overall residual in Fig. 5, suggesting that the aerosol ERF level was indeed too negative in the anthropogenic ERF time series used in Fig. 4. The aerosol and GHG scaling factors are correlated (Fig. S2), which is expected given the energy budget constraints set by GMST observations (for a given climate response parameter set, a large negative aerosol ERF estimate will correlate with a large positive GHG ERF estimate, in order to balance the historical energy budget). The level and rate of present-day anthropogenic warming are also correlated (Fig. S3 in the online supplemental material), with some of this correlation likely arising from the sampling methodology used to produce the ERF ensemble (discussed in section 2; see also Fig. S4 in the online supplemental material).

2) WARMING TRENDS POST-2000

What does Fig. 5 say about the contributions to recent GMST trends? Anthropogenic warming trends increase from +0.19 (0.14–0.24) °C decade^{-1} in 2000–09 to +0.24 (0.15–0.32) °C decade^{-1} in 2010–19. Aerosol-induced warming trends increase from +0.00 (−0.01–0.00) °C decade^{-1} in 2000–09 to +0.03 (0.00–0.07) °C decade^{-1}, contributing the majority of the overall anthropogenic warming acceleration. Aerosol and GHG warming trends show the same broad characteristics in Fig. 4b and the right panel of Fig. 5—early-twentieth-century GMST trends deviate from the anthropogenic warming trend, while early-twenty-first-century GMST trends are, in part, attributed to anthropogenic sources. However, the right panel of Fig. 5 attributes substantially less of this post-2000 GMST trend change to anthropogenic origins. While Fig. 4's best-estimate anthropogenic warming trend explains more than 80% of the GMST trend change since 2000, Fig. 5 (right panel) only explains around 50% of the GMST trend change with the anthropogenic ERF trend change (the 5th–95th percentile range is approximately 0%–100% of the GMST trend change being caused by anthropogenic influence), with the remainder being attributed to natural variability. A small number of ensemble members do continue to attribute the full GMST trend change to an anthropogenic ERF trend change, although substantially less of the distribution considers this a plausible explanation when compared with Fig. 4b where much higher 2010–19 anthropogenic warming trends were possible.

Reducing the aerosol ERF by around 40% in Fig. 5 results in a better reproduction of the GMST behavior over the historical record as a whole. Figures 4 and 5 are trading off using aerosol forcing to explain the post-2000 GMST behavior (including a larger aerosol ERF trend change) versus using aerosol forcing to explain mid-twentieth-century GMST

behavior (including a smaller ERF trend change). Rescaling the aerosol warming to fit mid-twentieth-century GMST automatically reduces the aerosol contribution to early twenty-first-century GMST trends too, since each component's ERF level correlates tightly with its ERF trend. In determining which of Figs. 4 or 5 better reflects historical aerosol contribution, we must weigh up the extent to which mid-twentieth-century GMST provides relevant information for constraining the aerosol warming trend post-2000, particularly given that midcentury forcing assessments are supported with substantially less observational evidence. For example, using aerosol ERF with *zero-trend-change* since 2000 (dashed lines in Fig. 2) to attribute warming contributions in Fig. 5 causes no substantial change in the quality of fit to GMSTs over the twentieth century, suggesting it is an acceptable explanation for historical GMST behavior, but substantially reduces the anthropogenic warming trend change since 2000 (orange and black dashed lines in Fig. 5).

Conversely, ignoring the mid-twentieth-century constraint entirely, Fig. 2's range of aerosol ERF trends supports a wider range of hypotheses, including aerosol trends entirely explaining GMST post-2000, or much of the trend change arising in response to internal variability alone. Clearly internal variability plays a substantial role in determining the trend over decadal and shorter time scales—the residuals in Fig. 4b and the right panel of Fig. 5 both show departures of around 0.1°–0.2°C decade^{-1} away from the anthropogenic decadal warming trend in the early twentieth century (Hegerl et al. 2018), and in Fig. 5 (right panel) much of the recent GMST trend change is again left unattributed to an external forcing source, suggesting an important role of ENSO and PDO variability here too (see Fig. 9, with the particularly strong El Niño event in 2015/16 highlighted) (Loeb et al. 2019).

In summary, GMST observations do appear to have accelerated since 2000 (Met Office 2013), with around 80% of this change attributed to aerosol ERF trend changes if the attribution uses the bulk anthropogenic ERF shape from Fig. 2. However, this anthropogenic ERF shape may not be the best description of the energy imbalance contributing to historical GMSTs. Biasing the aerosol ERF too negative causes the mid-twentieth-century anthropogenic warming to be low relative to GMST observations in Fig. 4. In Fig. 5 the aerosol and GHG contributions are separately attributed to the GMST anomaly, finding the best explanation of historical GMST by reducing the aerosol contribution by 40%. Figure 5 suggests around 50% of the post-2000 GMST acceleration is attributable to the anthropogenic ERF trend change (+0.05°C decade^{-1} between 2000–09 and 2010–19, of which +0.03°C decade^{-1} is because of aerosols, with the other +0.02°C decade^{-1} from GHGs). The remaining 50% of the GMST acceleration is attributed to unforced internal variability. If the attribution focuses on trends post-2000 alone then there is greater freedom: although recent GMST trend changes may originate from anthropogenic ERF trends in isolation, PDO and ENSO signals covary substantially over the period, meaning credible counterhypotheses include a smaller aerosol ERF trend change assumption since 2000 with GMST trend change arising largely from internal variability.

c. *TOA radiative fluxes*

Further assessing the extent of PDO and ENSO's influence on recent GMST requires separating the contributions from external forcing, temperature-mediated feedbacks, and internal variability. Studying the TOA flux trend change over the past two decades provides a means to measure the internal variability contribution to recent changes in the rate of warming.

In Fig. 6 we display radiative flux anomalies from Earth observations since 2000, and various simulations of the recent historical period using GCMs. The left column plots the observed globally averaged outgoing flux anomaly recorded by CERES (Loeb et al. 2017) between 2000 and 2020. Figures 6a–c show the longwave (LW) TOA flux anomaly in red, the shortwave (SW) TOA flux anomaly in orange, and the net TOA flux anomaly in black, respectively; in all panels dotted lines refer to clear-sky anomalies, and solid lines to all-sky anomalies. In all panels a shaded region (2000–12) highlights the period commonly considered to exhibit the so-called pause in global warming. Also in Fig. 6 are atmosphere-only simulations with prescribed SSTs using the *historical*+SSP3-70 scenario (middle column) and coupled atmosphere–ocean simulations using a *historical*+SSP2-45 scenario (right column), which allow us to explore scenarios that have removed the externally applied ERF trend change and internal variability contributions to TOA flux trend behavior, respectively.

1) The net TOA flux anomaly

The net flux in Fig. 6c has a negative trend (-0.44 ± 0.20 W m^{-2} decade^{-1}) that remains approximately constant over the two-decade interval. Compare these net TOA flux trends with those produced over the same 20-yr interval in a prescribed-SST atmosphere-only *historical*+SSP3-70 experiment using the CESM2 model (Fig. 6f), and with an ensemble of coupled atmosphere–ocean models running with *historical*+SSP2-45 forcing (Fig. 6i). These two experiments isolate the key trend drivers in the observations: the prescribed-SST *historical*+SSP3-70 experiment has minimal trend change induced by a change in aerosol emissions (SSP3-70 has the smallest aerosol ERF trend change; see Fig. 3) but captures responses caused by the SST boundary conditions, whereas the coupled simulations remove the trend change arising due to SST variability by averaging over an ensemble of responses, but include the SSP2-45 anthropogenic ERF trend change signal (shown in Fig. 2).

The decadal trends identified are larger for the observations (Fig. 6c) and for the atmosphere-only prescribed-SST experiments (Fig. 6f), relative to the coupled-model ensemble (Fig. 6i), consistent with the net feedback parameter being biased by short-term variability processes. The prescribed-SST experiment in Fig. 6f is not a perfect reproduction of observations (particularly noting the trend with the opposite sign identified in the first decade), although the key variability is captured (e.g., high TOA flux peak in 2010/11) and the experiment appears to approximately reproduce the behavior of the net TOA flux anomaly (comparing the pink lines in Figs. 6c and 6f). The trend change in Fig. 6i (-0.2 W m^{-2} decade^{-1} between the first and second decade) shows the average impact

of the *historical*+SSP2-45 anthropogenic ERF trend change on net TOA flux trends isolated from internal variability processes.

To determine whether the trends identified in Figs. 6c, 6f, and 6i are consistent with the anthropogenic forcing time series in Fig. 2 we can regress the forcing-adjusted TOA flux anomaly [$F - N$ in Eq. (1)] against GMST. The gradient of this fit is an estimate of the net feedback parameter, which we can compare across the experiments and with alternative observational constraints to infer the influence of internal variability on the TOA flux record in the past two decades. The ensemble-mean net feedback parameter in Fig. 6i is +1.1 W m^{-2} °C^{-1}, consistent with the estimated feedback strength in 4 × CO_2 experiments (Flynn and Mauritsen 2020).

Estimating the net feedback parameter in this way using observations can introduce a bias because short-term internal variability influences the TOA flux anomaly trend (Dessler and Forster 2018), meaning the feedback parameter may not reflect the true value of the multicentury equilibrium climate sensitivity. An unbiased estimate of the net feedback strength over a short observational record using a total least squares regression would require an external estimate of the total variance in GMST and TOA flux observations, including partitioning between the various sources of variability. This partitioning is extremely challenging to characterize over the historical record, with a poor understanding of drivers of the variability in surface- and deep-ocean heat uptake, and of key temperature-mediated feedbacks (such as cloud cover variability over the tropical Pacific Ocean).

Despite this, many groups have attempted to estimate the net feedback parameter using short observational records with some success (Donohoe et al. 2014; Murphy et al. 2009). Similarities between their results and the expected multicentury feedback parameter likely stem from fortuitous cancellations in the key internal variability signals over the first decade of CERES observations (see ENSO and PDO values between 2000 and 2010 in Fig. 9). This is not the case over the full period 2000–20, which includes a strong El Niño event in 2015/16 and a negative-to-positive PDO shift.

Using the approach described in the datasets and methods section above (section 3a) we estimate of the net feedback parameter for observations in Fig. 6c, λ_{net}, finding $\lambda_{net} = +0.74 \pm 0.34$ W m^{-2} °C^{-1}. This net feedback parameter estimate is likely biased low by short-term natural variability: $\lambda_{net} \sim +1.2$ W m^{-2} °C^{-1} produces an equilibrium climate sensitivity (ECS) around 3°C, the best-estimate value in AR6 (Forster et al. 2021), assuming $F_{2\times CO_2}$, the forcing resulting to doubling CO_2 concentrations, is 3.74 W m^{-2}. Sherwood et al.'s recent reassessment of the ECS still includes substantial uncertainty ($\lambda_{net} = +1.3 \pm 0.44$ W m^{-2} °C^{-1}, with $F_{2\times CO_2} = +4.00 \pm 0.30$ W m^{-2}) (Sherwood et al. 2020). We can adjust our λ_{net} estimate using the mean CMIP5 relationship between decadal and multicentury feedback parameters, following Dessler and Forster (2018), to attempt to account for this bias. This finds a best-estimate $\lambda_{net} = +0.92$ W m^{-2} °C^{-1}, which corresponds to an ECS around 4°C, in the upper half of the uncertainty range in the AR6, but consistent with other observationally constrained studies (Donohoe et al. 2014; Murphy et al. 2009; Dessler and Forster 2018).

Another option to account for the variability signal uses a joint regression of NOAA's Niño-3 index, PDO index (NOAA 2019) and surface temperature anomalies onto forcing-adjusted fluxes, with the aim of identifying the ENSO and PDO variability contributions to the feedback parameter. This finds $\lambda_{net} = +0.85 \pm 0.44$ W m^{-2} °C^{-1}, shifting in the correct direction but remaining lower than the multicentury feedback strength (similar to the CMIP5-adjusted response above). This joint regression approach finds relatively weak correlation between ENSO or PDO and the net flux anomaly, despite the impact of ENSO on tropical Pacific cloud cover being highlighted as a key driver of net TOA flux variability (Loeb et al. 2019; Masson-Delmotte et al. 2021). This failure to correlate ENSO or PDO variability with the net flux trend change likely arises due to the large variability in Fig. 6c, which dominates over the scale of the ENSO/PDO trends, along with the fact that SST variability itself correlates well with the ENSO record over these intervals (Loeb et al. 2021). This demonstrates the challenge in determining the partitioning of variances contributing the observed TOA flux anomaly, and means that the quality of feedback parameter fits do not in and of themselves represent evidence supporting or refuting recent ERF trends.

2) Separating the SW and LW contributions

Additional insight can be gained by separating the TOA flux anomaly into shortwave and longwave contributions, plotted in Figs. 6a and 6b. As with the net TOA flux record in Fig. 6c, the influence of internal variability on the measured LW and SW feedback parameters is used to gain an understanding of the likely contribution to trends in the LW and SW records over the last two decades. We expect the SW component trends to be a key indicator of the aerosol contribution, since aerosols principally interact with SW radiation both directly and through aerosol–cloud interactions.

Over the first decade (2000–09), the LW flux anomaly exhibits a near-zero trend (0.0 ± 0.1 W m^{-2} decade^{-1}), with the weak positive GMST trend and a steadily increasing LW ERF (principally from the ongoing CO_2 emissions radiative contribution; see Fig. 2). Over the second decade (2010–19) the LW flux anomaly trend is positive (+0.9 ± 0.2 W m^{-2} decade^{-1}), with continuing GHG ERF trends combining with a strong positive GMST trend.

A subset of the CERES dataset excluding particularly strong El Niño events (defined as having a Niño-3 index greater than 2.0, highlighted in Fig. 9) produces a LW feedback parameter characteristic of the multidecade "noise-free" response ($\lambda_{LW,masked} = +2.2 \pm 0.3$ W m^{-2} °C^{-1}), in agreement with Donohoe et al. (2014), who estimate the LW feedback parameter using CERES data up to December 2013. (Donohoe's feedback parameter estimates use a period of CERES observations absent in major swings in ENSO and PDO variability, so the estimates are generally more consistent with expected multicentury values than those calculated over periods including the 2015/16 El Niño event.) A slightly

larger feedback parameter is obtained if all data are included ($\lambda_{LW} = +2.3 \pm 0.2$ W m^{-2} °C^{-1}). Both of these estimates are consistent with previous efforts to deduce the LW feedback parameter using observations but are slightly larger than those found using GCMs running a 4 × CO_2 experiment ($\lambda_{LW} = +1.8 \pm 0.5$ W m^{-2} °C^{-1}) (Flynn and Mauritsen 2020) or using the mean coupled-model response in Fig. 6g ($\lambda_{LW} = +1.9$ W m^{-2} °C^{-1}).

The observed SW flux anomaly has a similarly large trend change between the first and second decades in Fig. 6b, but in the opposite direction to the LW response (from -0.4 ± 0.2 W m^{-2} decade^{-1} between 2000 and 2010 to -1.2 ± 0.3 W m^{-2} decade^{-1} between 2010 and 2020). Estimates of the SW feedback parameter are more uncertain than their LW equivalent, principally due to a continued poor knowledge of how cloud–aerosol interactions vary under changing aerosol emissions pattern and under a changing background climate state (Forster et al. 2021). However, recent work claims to have ruled out negative cloud feedbacks, in effect ruling out very strong SW feedbacks and hence very small ECS values (Ceppi and Nowack 2021).

Uncertainty in the measurement of the SW feedback is further confounded when combined with the covarying natural variability signals in Fig. 6b. Since 2000, the PDO and ENSO have driven much of the variability in tropical cloud cover (Loeb et al. 2019), key to the resulting SW flux trends (Loeb et al. 2021). Observed reductions in sea ice cover (Notz and Stroeve 2016) may also contribute to the trends observed in Fig. 6b, although the cloud fraction variability and major El Niño event in 2015/16 are the major drivers of SW flux variability (Loeb et al. 2019). As with the LW anomaly, the SW feedback parameter can be estimated using the entire CERES SW record (2000–20), or subsetting to mask out the most significant ENSO variability. The full record's $\lambda_{SW} = -1.6 \pm 0.3$ W m^{-2} °C^{-1}, larger than the SW feedback measured in GCMs over multicentury intervals. Masking the prominent 2015/16 El Niño years finds $\lambda_{SW,masked} = -1.2 \pm 0.3$ W m^{-2} °C^{-1}. A joint regression of ENSO, PDO, and temperature anomalies onto the SW flux anomaly finds $\lambda_{SW} = -1.4 \pm 0.4$ W m^{-2} °C^{-1}. As with the LW feedback, this joint regression finds only a limited contribution from ENSO explicitly, predominantly because of the correlation between the global-averaged SSTs and ENSO variability (Loeb et al. 2019). Removing the impact of internal variability completely gives $\lambda_{SW} = -0.8 \pm 0.5$ W m^{-2} °C^{-1} using 4 × CO_2 experiments (Flynn and Mauritsen 2020) or $= -1.0$ W m^{-2} °C^{-1} using the mean coupled-model response in Fig. 6h.

We compare the observed LW and SW flux anomaly behavior in Figs. 6a and 6b with the low-aerosol-trend-change SSP3-70 and prescribed-SSTs experiment (Figs. 6d,e), and the ensemble-mean SSP2-45 experiment that averages out the impact of SST and cloud cover variability (Figs. 6g,h). In the experiments where internal variability has been removed the decadal trends show much smaller trend changes than the CERES observations, while the prescribed-SST experiment continues to show a large change in the decadal trend despite having a small aerosol ERF trend change. This supports the assessment that trends in the left column's anomalies are significantly exaggerated in response to short-term variability signals, as is proposed in our analysis of observed feedback parameters and in the attribution of the aerosol ERF contribution to the GMST trend change above. The LW flux anomaly trend change is reasonably well reproduced in the multimodel ensemble average response, reinforcing the claim that the GHG contribution to the TOA flux anomaly is well understood over this period as a combination of the externally forced response (including various LW temperature-mediated feedbacks) and internal variability (Fig. 6d). The SW trend change is almost entirely missed in the ensemble-average coupled model response of Fig. 6h, suggesting that the vast majority of the SW trend change occurs due to natural variability (driven by SST variability) and not because of aerosol ERF trend changes. A wide range of aerosol ERF trend changes are therefore compatible with the observed SW trend change in Fig. 6b, including zero trend change over the interval.

CERES observations suggest a larger LW feedback over the past two decades than CMIP6 GCMs (cf. the trends in Figs. 6a and 6g), although within the range of uncertainty (Flynn and Mauritsen 2020). This may result from natural variability influencing LW fluxes in observations, by varying sea surface temperatures or the rate of ocean heat uptake. However, this does go against the notion that natural variability will principally bias SW feedbacks through variations in cloud cover (Loeb et al. 2019) and recent updates to ocean heat uptake datasets, which show a roughly constant trend over the past two decades (Zanna et al. 2019). One alternative explanation for the discrepancy is that LW fluxes are partly increased since 2000 because of an additional LW cloud-ice feedback in response to the declining atmospheric aerosol burden as anthropogenic aerosol emissions decrease. LW fluxes have been demonstrated to increase in response to reduced upper-tropospheric cloud ice content, which occurs following aerosol emissions reductions in regional CRM simulations (Dagan et al. 2020; Marinescu et al. 2021). This additional LW feedback to aerosol emissions perturbations is not captured in the GCM's parameterized convection schemes at present, hence the possibility for discrepancy between observations and coupled models.

In summary, the decadal TOA flux trends assessed from CMIP6 models are consistent with the ERF trends in Fig. 2, and ensemble averages over CMIP6 coupled model runs provide an assessment of the underlying forced response behavior we should hunt for in observations. Much larger trend changes are identified in observed LW and SW TOA flux anomalies than those predicted by anthropogenic ERF trends alone (cf. Figs. 6a,b with Figs. 6g,h). The observed trend changes are better explained as resulting from SST and cloud cover variability since 2000; CESM2's AMIP *historical*+SSP3-70 ensemble supports this assessment (Figs. 6d,e), with larger trends appearing in the flux anomalies when the model is run with observed SSTs over the interval, despite the experiment also containing a much smaller anthropogenic ERF trend change. The best-estimate ERF time series does explain the TOA flux observations behavior shown in the left column of Fig. 6. However, as

we determined in the GMST analysis, a wide range of near-term ERF trends is plausible since the principal driver of changes in the TOA flux trend since 2000 is likely SST and cloud cover variability, and not changes in the aerosol ERF trend.

d. Aerosol optical depths

Global AOD observations (black) are remarkably stable since 2000 in the left panel of Fig. 7 (the period 1995–2000 shows a trend from the 1991 Mount Pinatubo eruption). Separating the Northern Hemisphere (NH) AOD trends isolates a slight peak-and-decline behavior since 2000 (red), while the global average is dampened by a flatter and smaller Southern Hemisphere (SH) AOD contribution (blue). Since anthropogenic aerosol emissions are predominantly released in the NH, this weak SH trend reflects the near-constant natural AOD contribution over the two-decade period of AOD observations. Regional anomalies in the right panel of Fig. 7 more clearly show emissions-induced trends in Southeast Asia, which are to first order balanced by an accelerating trend in northern Africa in this dataset (and smaller contributions from Australia and South America). Regional SO_2 emissions time series in Fig. 1 corroborate these Southeast Asian AOD trends, but there is little evidence supporting an acceleration of North African AOD caused by anthropogenic emissions in emissions datasets. Limited in situ observations and high variability in Aeronet AODs (Sogacheva et al. 2020) mean validation is challenging. Based on a global linear emissions-to-AOD relationship (see section 3a), Fig. 1 suggests that the anthropogenic AOD anomaly should have declined by around a third since 2000.

In Fig. 7, the difference between the NH (red) and SH (blue) AOD time series provides an estimate of the NH's anthropogenic AOD anomaly (we assume that the SH component contains a negligible anthropogenic component, and therefore acts as a proxy for the NH's natural AOD contribution). Differencing the NH and SH AOD time series finds a subtle peak-and-decline trend change, with a 10%–30% decrease in the NH anthropogenic AOD anomaly between 2010 and 2018. This NH trend supports the SO_2 emissions behavior exhibited in Fig. 1, but it is approximately halved in the global average since little anthropogenic AOD is contributed by the SH. GCMs are shown to replicate the observed emissions-to-AOD relationship in the global and hemispheric average (see, e.g., the AOD anomalies produced from CMIP6 models historical experiments in Fig. S7 of the online supplemental material).

The fact that anthropogenic aerosol emissions are largely localized in the NH reduces the percentage change in global AOD that we observe for a given percentage change in aerosol emissions. This is contrary to the estimated aerosol ERF percentage change, which is reasonably large in Fig. 2. This lack of coherence between observables along the aerosol chain from emissions to AOD to ERF could be indicative of a pattern dependence for aerosol emissions, where the spatial distribution of emissions impacts on their global-average ERF outcome. Some research suggests that the spatial distribution of aerosol emissions will alter the efficacy and lifetime of atmospheric aerosol perturbations, complicating the prospect of simple global emissions-to-AOD relationship described above (Kasoar et al. 2018; Sand et al. 2020; Persad and Caldeira 2018). The size of this impact requires further research.

Despite these concerns there has been success working within a global linear framework for the relationship between SO_2 emissions and aerosol ERF (Bellouin et al. 2020). Below we look to the behavior of CMIP6 models to study the global AOD-to-ERF relationship.

Trends in global AOD and ERF

To establish whether the gradient change in observed AOD is consistent with Fig. 2's global aerosol ERF trends, Fig. 8 plots the decadal linear trend change (2010–20 minus 2000–10) in AOD (Fig. 8a) and ERF (Fig. 8b). For the five CMIP6 models the AOD trend change over the two decades since 2000 lies between -0.011 and -0.023 decade^{-1} (black scatter points in Fig. 8a), while Fig. 7's observed AOD trends change by between -0.002 and -0.029 decade^{-1}. NH trends dominate the global trends in the CMIP6 models as they did for observations (shown in red on Fig. 8a, with individual model trendlines shown in the online supplemental material) and are modulated by weaker SH trends (blue scatter points in Fig. 8a).

The relative change in CMIP6 ERF trends (shown in Fig. 8b) are more uncertain than corresponding CMIP6 AOD trends, reflecting the greater difficulty in assessing the downstream properties of the climate system that become increasingly impacted by natural variability. We compare the assessed CMIP6 ERF trend change with three estimates of the ERF trend change from Fig. 2 in Fig. 8b, labeled "Aerosol ERF". The orange range shows the estimated ERF trend change directly lifted from Fig. 3 (the inner range shows SSP2-45's aerosol ERF trend change and the wider range the full range across all SSP variants). In black and blue are two alterative estimates of Fig. 2's aerosol ERF trend change: blue is the difference between the 2010–19 and 2000–09 linear trends (consistent with the method used to derive AOD trend change estimates for the CMIP6 models in Fig. 8) and black is the difference between the 2010–19 and 1990–2009 linear trends.

Figure 2's aerosol ERF trend change (orange) overlaps with the trend change calculated for the five CMIP6 models ERFs shown in Fig. 8b. However, while Fig. 2's ERF trend change consistently produces positive aerosol ERF trend changes since 2000, the five CMIP6 models often have aerosol ERF trend changes that overlap with zero, despite the model-derived AOD trend change estimates all being negative over the same interval.

If we assume that a linear relationship exists between the AOD trend change and the aerosol ERF trend change (i.e., a single efficacy parameter governs the relationship between Figs. 8a and 8b, defined using the ensemble-mean CMIP6 response), we can estimate the ERF trend change we would expect, given the AOD trend change that has been observed since 2000. This "AOD-ERF consistent range" in Fig. 8b finds a wider range of aerosol ERF trends is compatible with observed AODs since 2000, expanding beyond the estimates

from the standard ERF trends assessed in Fig. 2 to also include both near-zero trend change and higher trend changes. While this higher limit is not supported by CMIP6 models themselves (the upper end of the range far exceeds the limits of the individual CMIP6 model fits), near-zero trend change is also observed in individual model outputs in Fig. 9b, implying a no-trend-change aerosol ERF scenario is plausible in both modeled and observed AOD responses since 2000.

4. Consequences of alternative aerosol forcing trends

Successive IPCC reports have given assessments of the level of anthropogenic global warming, but no equivalent assessment of the rate of human-induced warming has been made. This is despite the rate of warming offering arguably more policy relevance at the present day in determining the time remaining to key goals of the Paris Agreement. This study highlights the key contributors to a perceived acceleration in the anthropogenic rate of warming since 2000 and uses observations of the climate system to constrain the forced response. Section 2 breaks down an ERF dataset that suggests anthropogenic ERF accelerated between 2000 and 2020, shown to arise because of aerosol forcing trends becoming positive around 2010 in the ERF ensemble. In section 3 we then step through three observational records to search for evidence supporting this assessed trend change.

Global temperatures show a clear change in trend between 2000 and 2020, characterized by temperatures remaining stable at around +1.0°C above preindustrial levels in the first decade, whereas in the second decade temperatures increase rapidly (with the rate of warming peaking at over +0.3°C decade^{-1}). The reduced warming trend around 2000 has been discussed in the context of ocean heat uptake and natural variability (Masson-Delmotte et al. 2021; IPCC et al. 2013), but less research has focused on a possible warming acceleration in the following decade induced by aerosol ERF trend changes. By attributing the temperature trends to anthropogenic and natural ERFs we show that the forcing time series from Fig. 2 capture the broad warming contributions over the previous two decades (Fig. 4). However, significant variations around the anthropogenic best fit are still present (e.g., see the period of early Arctic warming in Fig. 4a), and alternative forcing trend change assumptions can be applied with little indication of a worse fit. A three-way regression isolates the aerosol contribution over history in Fig. 5, fitting the mid-twentieth-century GMST more successfully by downscaling the aerosol contribution. Hence, the aerosol ERF trend change contribution since 2000 is also downscaled, with best-estimate anthropogenic warming trend change around +0.05°C decade^{-1} between 2000–09 and 2010–19 (the 5th–95th-percentile range spans 0.01°–0.08°C decade^{-1}). The aerosol contribution to this is +0.03°C decade^{-1} between 2000–09 and 2010–19 (the 5th–95th-percentile range spans 0.00°–0.07°C decade^{-1}).

In the CERES record, LW TOA flux contributions are explained by recent GMST and forcing trends combined, while there is greater uncertainty in the contributors to the SW and net flux anomalies. In the SW anomaly, unforced variability in temperature and TOA flux time series precludes clear assessments of the aerosol ERF contribution, supporting the assessment that significant contributions from ENSO and PDO are present in recent TOA flux trend changes. Given this, TOA flux trends cannot rule out little to no anthropogenic ERF trend change over the two decades, despite the best-estimate anthropogenic ERF time series agreeing well with both TOA fluxes and temperature anomalies. Figure 6's middle column (atmosphere-only TOA flux anomalies) and right column (coupled-model TOA flux anomalies) confirm the major role played by natural variability processes in these TOA flux records, demonstrating that the trend change induced in the SW TOA flux anomaly, where we expect to observe a large trend change induced by aerosols (Fig. 6h), is small relative to the trend change caused by unforced variability over the previous two decades (Fig. 6e). Continued funding for new satellites to study the outgoing radiative balance of the Earth system (such as the recently announced FORUM mission; ESA 2021) is vitally important in order to maintain long-term records and constrain radiative feedbacks with greater certainty.

Satellite observations and CMIP6 models agree that a relatively small AOD trend change has occurred over the last two decades, despite significant reductions in anthropogenic aerosol emissions in the Northern Hemisphere. Exploring a linear relationship between AOD and aerosol ERF trends (based on the mean response of CMIP6 models) allows us to estimate the ERF trend change expected in response to the observed AOD trend change since 2000. This analysis again supports the best estimate ERFs in Fig. 2, but also suggests that little-to-no trend change remains a possible assessment for ERF trends since 2000 in observations. The spatial pattern of aerosol emissions also may play a role in determining the aerosol ERF level (Stier et al. 2013), causing nonlinearities in the AOD and ERF responses to globally averaged aerosol emissions reductions. Further research of ERF trends and feedbacks using their full spatiotemporal signal in AMIP GCM experiments where forcing time series are known, and conducting regional aerosol perturbation experiments in coupled models (Wilcox et al. 2022), will provide more insight.

Overall, this assessment suggests that aerosol emissions reductions have contributed to an increase in the rate of anthropogenic warming since 2000, but both to a lesser degree than is suggested in the ERFs presented in Fig. 2, and with a substantial uncertainty range including the possibility of little contribution over two decades. The forced behavior coincides with a period of considerable internal variability, meaning that isolating the aerosol-induced ERF trend change from observations is challenging, and that a wide range of ERF scenarios offer plausible explanations of the past 20 years. Some of these possibilities are not well represented in the ERF ensemble shown in Fig. 2: for example, a *zero-trend-change* aerosol ERF scenario between 2000 and 2020 (shown in Fig. 2 as an dashed orange line, with the corresponding anthropogenic ERF a black dashed line), is considered possible in the analysis of all three observation datasets but is not represented well in the ERF ensemble of Fig. 2. Using a *zero-trend-change* aerosol ERF to attribute the anthropogenic contribution to global warming results in a similar quality fit to GMSTs (see dashed orange and black lines in Fig. 5,

left panel), but substantially reduces the anthropogenic warming trend change that occurs since 2000 (orange and black dashed lines in Fig. 5, right panel). A comprehensive ERF ensemble of the recent time-history of anthropogenic ERF should offer these alternative scenarios, including scenarios with reduced aerosol ERF trend change since 2000 and with alternative rescalings for all pollutants using global energy balance constraints [e.g., those in Smith et al. (2021a) or Fig. 5].

The importance of continuing to track and constrain the early twenty-first century's forcing trends is underappreciated, and future work should focus on providing better constraints to near-term forcing trends as well as their levels. Short-term ERF trends are vital to accurately assess this decade's warming rate, with tangible, real-time impacts for global mitigation policy.

Acknowledgments. Author Jenkins acknowledges NERC grant NE/L002612/1 and support from the European Space Agency's Climate Change Initiative. Authors Stier, Allen, and Jenkins acknowledge funding from the FORCeS project under the European Union's Horizon 2020 research program with grant agreement 821205. Stier acknowledges funding from the European Research Council project RECAP under the European Union's Horizon 2020 research and innovation program with grant agreement 724602. Authors Grainger and Povey acknowledge NERC's support of the National Centre for Earth Observation, contract number PR140015. The National Center for Atmospheric Research is sponsored by the U.S. National Science Foundation. The authors thank Chris Smith for many insightful discussions on the preparation of ERF datasets and Nick Leach for discussions on FaIRv2.0.

Data availability statement. All observational datasets required for the analysis are available freely at the locations cited in the text. Code is available upon request to the corresponding author.

REFERENCES

Allen, M. R., and Coauthors, 2018: Chapter 1: Framing and context. *Special Report on Global Warming of 1.5°C*, Cambridge University Press, 49–92.

Bellouin, N., and Coauthors, 2020: Bounding global aerosol radiative forcing of climate change. *Rev. Geophys.*, **58**, e2019RG000660, https://doi.org/10.1029/2019RG000660.

Ceppi, P., and P. Nowack, 2021: Observational evidence that cloud feedback amplifies global warming. *Proc. Natl. Acad. Sci. USA*, **118**, e2026290118, https://doi.org/10.1073/pnas.2026290118.

Collins, W. J., and Coauthors, 2017: AerChemMIP: Quantifying the effects of chemistry and aerosols in CMIP6. *Geosci. Model Dev.*, **10**, 585–607, https://doi.org/10.5194/gmd-10-585-2017.

Dagan, G., P. Stier, M. Christensen, G. Cioni, D. Klocke, and A. Seifert, 2020: Atmospheric energy budget response to idealized aerosol perturbation in tropical cloud systems. *Atmos. Chem. Phys.*, **20**, 4523–4544, https://doi.org/10.5194/acp-20-4523-2020.

Dessler, A. E., and P. M. Forster, 2018: An estimate of equilibrium climate sensitivity from interannual variability. *J. Geophys. Res. Atmos.*, **123**, 8634–8645, https://doi.org/10.1029/2018JD028481.

Dong, Y., and Coauthors, 2021: Biased estimates of equilibrium climate sensitivity and transient climate response derived from historical CMIP6 simulations. *Geophys. Res. Lett.*, **48**, e2021GL095778, https://doi.org/10.1029/2021GL095778.

Donohoe, A., K. C. Armour, A. G. Pendergrass, and D. S. Battisti, 2014: Shortwave and longwave radiative contributions to global warming under increasing CO_2. *Proc. Natl. Acad. Sci. USA*, **111**, 16 700–16 705, https://doi.org/10.1073/pnas.1412190111.

ESA, 2021: A new satellite to understand how Earth is losing its cool. Accessed 13 December 2021, https://www.esa.int/Applications/Observing_the_Earth/A_new_satellite_to_understand_how_Earth_is_losing_its_cool.

Eyring, V., S. Bony, G. A. Meehl, C. A. Senior, B. Stevens, R. J. Stouffer, and K. E. Taylor, 2016: Overview of the Coupled Model Intercomparison Project phase 6 (CMIP6) experimental design and organization. *Geosci. Model Dev.*, **9**, 1937–1958, https://doi.org/10.5194/gmd-9-1937-2016.

Flynn, C. M., and T. Mauritsen, 2020: On the climate sensitivity and historical warming evolution in recent coupled model ensembles. *Atmos. Chem. Phys.*, **20**, 7829–7842, https://doi.org/10.5194/acp-20-7829-2020.

Forster, P. M., and Coauthors, 2016: Recommendations for diagnosing effective radiative forcing from climate models for CMIP6. *J. Geophys. Res. Atmos.*, **121**, 12 460–12 475, https://doi.org/10.1002/2016JD025320.

——, and Coauthors, 2021: The Earth's energy budget, climate feedbacks, and climate sensitivity. *Climate Change 2021: The Physical Science Basis*, V. Masson-Delmotte et al., Eds., Cambridge University Press, 923–1054, doi:10.1017/9781009157896.009.

Friedlingstein, P., and Coauthors, 2020: Global carbon budget 2020. *Earth Syst. Sci. Data*, **12**, 3269–3340, https://doi.org/10.5194/essd-12-3269-2020.

——, and Coauthors, 2022: Global carbon budget 2021. *Earth Syst. Sci. Data*, **14**, 1917–2005, https://doi.org/10.5194/essd-14-1917-2022.

Gettelman, A., and Coauthors, 2019: High climate sensitivity in the Community Earth System Model version 2 (CESM2). *Geophys. Res. Lett.*, **46**, 8329–8337, https://doi.org/10.1029/2019GL083978.

Gillett, N. P., and Coauthors, 2021: Constraining human contributions to observed warming since the pre-industrial period. *Nat. Climate Change*, **11**, 207–212, https://doi.org/10.1038/s41558-020-00965-9.

Hasselmann, K., 1997: Multi-pattern fingerprint method for detection and attribution of climate change. *Climate Dyn.*, **13**, 601–611, https://doi.org/10.1007/s003820050185.

Haustein, K., M. R. Allen, P. M. Forster, F. E. L. Otto, D. M. Mitchell, H. D. Matthews, and D. J. Frame, 2017: A real-time global warming index. *Sci. Rep.*, **7**, 15417, https://doi.org/10.1038/s41598-017-14828-5.

Hegerl, G. C., H. von Storch, K. Hasselmann, B. D. Santer, U. Cubasch, and P. D. Jones, 1996: Detecting greenhouse-gas-induced climate change with an optimal fingerprint method. *J. Climate*, **9**, 2281–2306, https://doi.org/10.1175/1520-0442(1996)009<2281:DGGICC>2.0.CO;2.

——, S. Brönnimann, A. Schurer, and T. Cowan, 2018: The early 20th century warming: Anomalies, causes, and consequences. *Wiley Interdiscip. Rev.: Climate Change*, **9**, e522, https://doi.org/10.1002/wcc.522.

Huang, B., and Coauthors, 2017: Extended Reconstructed Sea Surface Temperature, version 5 (ERSSTv5): Upgrades, validations, and intercomparisons. *J. Climate*, **30**, 8179–8205, https://doi.org/10.1175/JCLI-D-16-0836.1.

IPCC, 2013: Summary for policymakers. *Climate Change 2013: The Physical Science Basis*, T. F. Stocker et al., Eds., Cambridge University Press, 3–29.

——, 2018: Summary for policymakers. *Special Report on Global Warming of 1.5°C*. V. Masson-Delmotte et al., Eds., Cambridge University Press, 3–24, https://doi.org/10.1017/9781009157940.001.

Kasoar, M., D. Shawki, and A. Voulgarakis, 2018: Similar spatial patterns of global climate response to aerosols from different regions. *npj Climate Atmos. Sci.*, **1**, 12, https://doi.org/10.1038/s41612-018-0022-z.

Kovilakam, M., L. W. Thomason, N. Ernest, L. Rieger, A. Bourassa, and L. Millán, 2020: The Global Space-based Stratospheric Aerosol Climatology (version 2.0): 1979–2018. *Earth Syst. Sci. Data*, **12**, 2607–2634, https://doi.org/10.5194/essd-12-2607-2020.

Kramer, R. J., H. He, B. J. Soden, L. Oreopoulos, G. Myhre, P. M. Forster, and C. J. Smith, 2021: Observational evidence of increasing global radiative forcing. *Geophys. Res. Lett.*, **48**, e2020GL091585, https://doi.org/10.1029/2020GL091585.

Leach, N. J., and Coauthors, 2021: FaIRv2.0.0: A generalized impulse response model for climate uncertainty and future scenario exploration. *Geosci. Model Dev.*, **14**, 3007–3036, https://doi.org/10.5194/gmd-14-3007-2021.

Le Quéré, C., and Coauthors, 2020: Temporary reduction in daily global CO_2 emissions during the COVID-19 forced confinement. *Nat. Climate Change*, **10**, 647–653, https://doi.org/10.1038/s41558-020-0797-x.

Loeb, N. G., and Coauthors, 2017: Clouds and the Earth's Radiant Energy System (CERES) Energy Balanced and Filled (EBAF) Top-of-Atmosphere (TOA) edition-4.0 data product. *J. Climate*, **31**, 895–918, https://doi.org/10.1175/JCLI-D-17-0208.1.

——, H. Wang, F. G. Rose, S. Kato, W. L. Smith, and S. Sun-Mack, 2019: Decomposing shortwave top-of-atmosphere and surface radiative flux variations in terms of surface and atmospheric contributions. *J. Climate*, **32**, 5003–5019, https://doi.org/10.1175/JCLI-D-18-0826.1.

——, G. C. Johnson, T. J. Thorsen, J. M. Lyman, F. G. Rose, and S. Kato, 2021: Satellite and ocean data reveal marked increase in Earth's heating rate. *Geophys. Res. Lett.* **48**, e2021GL093047, https://doi.org/10.1029/2021GL093047.

Marinescu, P. J., and Coauthors, 2021: Impacts of varying concentrations of cloud condensation nuclei on deep convective cloud updrafts—A multimodel assessment. *J. Atmos. Sci.*, **78**, 1147–1172, https://doi.org/10.1175/JAS-D-20-0200.1.

Masson-Delmotte, V., and Coauthors, 2021: Summary for policymakers. *Climate Change 2021: The Physical Science Basis*, Cambridge University Press, 6 pp.

McDuffie, E. E., and Coauthors, 2020: A global anthropogenic emission inventory of atmospheric pollutants from sector- and fuel-specific sources (1970–2017): An application of the Community Emissions Data System (CEDS). *Earth Syst. Sci. Data*, **12**, 3413–3442, https://doi.org/10.5194/essd-12-3413-2020.

Meinshausen, M., and Coauthors, 2020: The Shared Socio-Economic Pathway (SSP) Greenhouse gas concentrations and their extensions to 2500. *Geosci. Model Dev.*, **13**, 3571–3605, https://doi.org/10.5194/gmd-13-3571-2020.

Met Office, 2013: The recent pause in global warming (2): What are the potential causes? Met Office Rep., 24 pp., https://www.metoffice.gov.uk/binaries/content/assets/metofficegovuk/pdf/research/climate-science/climate-observations-projections-and-impacts/paper2_recent_pause_in_global_warming.pdf.

Millar, R. J., Z. R. Nicholls, P. Friedlingstein, and M. R. Allen, 2017: A modified impulse-response representation of the global near-surface air temperature and atmospheric concentration response to carbon dioxide emissions. *Atmos. Chem. Phys.*, **17**, 7213–7228, https://doi.org/10.5194/acp-17-7213-2017.

Morice, C. P., and Coauthors, 2021: An updated assessment of near-surface temperature change from 1850: The HadCRUT5 data set. *J. Geophys. Res. Atmos.*, **126**, e2019JD032361, https://doi.org/10.1029/2019JD032361.

Moseid, K. O., and Coauthors, 2020: Bias in CMIP6 models as compared to observed regional dimming and brightening. *Atmos. Chem. Phys.*, **20**, 16 023–16 040, https://doi.org/10.5194/acp-20-16023-2020.

Murphy, D. M., S. Solomon, R. W. Portmann, K. H. Rosenlof, P. M. Forster, and T. Wong, 2009: An observationally based energy balance for the Earth since 1950. *J. Geophys. Res.*, **114**, D17107, https://doi.org/10.1029/2009JD012105.

Myhre, G., and Coauthors, 2013: Anthropogenic and natural radiative forcing. *Climate Change 2013: The Physical Science Basis*, T. F. Stocker et al., Eds., Cambridge University Press, 659–740.

NASA Goddard Institute for Space Studies, 2018: GISS Surface Temperature Analysis (GISTEMP), version 4. Accessed 1 May 2018, https://data.giss.nasa.gov/gistemp.

NOAA, 2019: Climate at a glance. National Centers for Environmental Information (NCEI), accessed 4 October 2019, https://www.ncdc.noaa.gov/cag/global/time-series.

——, 2021a: Global Monitoring Laboratory – Carbon Cycle Greenhouse Gases. Accessed 10 March 2021, https://www.esrl.noaa.gov/gmd/ccgg/trends/.

——, 2021b: Climate Timeseries: Nino 3: NOAA Physical Sciences Laboratory. Accessed 8 June 2021, https://psl.noaa.gov/data/timeseries/monthly/NINO3/.

——, 2021c: NOAA AVHRR equipment and datasets. https://www.usgs.gov/centers/eros/science/usgs-eros-archive-advanced-very-high-resolution-radiometer-avhrr?qt-science_center_objects=0#qt-science_center_objects.

Notz, D., and J. Stroeve, 2016: Observed Arctic sea-ice loss directly follows anthropogenic CO_2 emission. *Science*, **354**, 747–750, https://doi.org/10.1126/science.aag2345.

Persad, G. G., and K. Caldeira, 2018: Divergent global-scale temperature effects from identical aerosols emitted in different regions. *Nat. Commun.*, **9**, 3289, https://doi.org/10.1038/s41467-018-05838-6.

Pincus, R., P. M. Forster, and B. Stevens, 2016: The Radiative Forcing Model Intercomparison Project (RFMIP): Experimental Protocol for CMIP6. *Geosci. Model Dev.*, **9**, 3447–3460, https://doi.org/10.5194/gmd-9-3447-2016.

Poulsen, C. A., and Coauthors, 2020: Cloud-cci ATSR-2 and AATSR dataset version 3: A 17-year climatology of global cloud and radiation properties. *Earth Syst. Sci. Data*, **12**, 2121–2135, https://doi.org/10.5194/essd-12-2121-2020.

Raghuraman, S. P., D. Paynter, and V. Ramaswamy, 2021: Anthropogenic forcing and response yield observed positive trend in Earth's energy imbalance. *Nat. Commun.*, **12**, 4577, https://doi.org/10.1038/s41467-021-24544-4.

Rao, S., and Coauthors, 2017: Future air pollution in the shared socio-economic pathways. *Global Environ. Change*, **42**, 346–358, https://doi.org/10.1016/j.gloenvcha.2016.05.012.

Rayner, N. A., D. E. Parker, E. B. Horton, C. K. Folland, L. V. Alexander, D. P. Rowell, E. C. Kent, and A. Kaplan, 2003: Global analyses of sea surface temperature, sea ice, and night marine air temperature since the late nineteenth century. *J. Geophys. Res.*, **108**, 4407, https://doi.org/10.1029/2002JD002670.

Ribes, A., S. Qasmi, and N. P. Gillett, 2021: Making climate projections conditional on historical observations. *Sci. Adv.*, **7**, eabc0671, https://doi.org/10.1126/sciadv.abc0671.

Rohde, R. A., and Z. Hausfather, 2020: The Berkeley Earth land/ocean temperature record. *Earth Syst. Sci. Data*, **12**, 3469–3479, https://doi.org/10.5194/essd-12-3469-2020.

Sand, M., T. K. Berntsen, A. M. L. Ekman, H.-C. Hansson, and A. Lewinschal, 2020: Surface temperature response to regional black carbon emissions: Do location and magnitude matter? *Atmos. Chem. Phys.*, **20**, 3079–3089, https://doi.org/10.5194/acp-20-3079-2020.

Sellar, A. A., and Coauthors, 2019: UKESM1: Description and evaluation of the U.K. Earth System Model. *J. Adv. Model. Earth Syst.*, **11**, 4513–4558, https://doi.org/10.1029/2019MS001739.

Sherwood, S. C., and Coauthors, 2020: An assessment of Earth's climate sensitivity using multiple lines of evidence. *Rev. Geophys.*, **58**, e2019RG000678, https://doi.org/10.1029/2019RG000678.

Shindell, D. T., A. Voulgarakis, G. Faluvegi, and G. Milly, 2012: Precipitation response to regional radiative forcing. *Atmos. Chem. Phys.*, **12**, 6969–6982, https://doi.org/10.5194/acp-12-6969-2012.

Smith, C., 2020: SSP ERF Timeseries. Accessed 23 September 2020, https://doi.org/10.5281/zenodo.3973015.

——, P. M. Forster, M. Allen, N. Leach, R. J. Millar, G. A. Passerello, and L. A. Regayre, 2018: FAIR v1.3: A simple emissions-based impulse response and carbon cycle model. *Geosci. Model Dev.*, **11**, 2273–2297, https://doi.org/10.5194/gmd-11-2273-2018.

——, and Coauthors, 2021a: Energy budget constraints on the time history of aerosol forcing and climate sensitivity. *J. Geophys. Res. Atmos.*, **126**, e2020JD033622, https://doi.org/10.1029/2020JD033622.

——, and Coauthors, 2021b: The Earth's energy budget, climate feedbacks, and climate sensitivity supplementary material. *Climate Change 2021: The Physical Science Basis*, V. Masson-Delmotte et al., Eds., available from https://www.ipcc.ch/.

Smith, T. M., R. W. Reynolds, T. C. Peterson, and J. Lawrimore, 2008: Improvements to NOAA's historical merged land–ocean surface temperature analysis (1880–2006). *J. Climate*, **21**, 2283–2296, https://doi.org/10.1175/2007JCLI2100.1.

Sogacheva, L., and Coauthors, 2020: Merging regional and global aerosol optical depth records from major available satellite products. *Atmos. Chem. Phys.*, **20**, 2031–2056, https://doi.org/10.5194/acp-20-2031-2020.

Stevens, B., 2015: Rethinking the lower bound on aerosol radiative forcing. *J. Climate*, **28**, 4794–4819, https://doi.org/10.1175/JCLI-D-14-00656.1.

Stier, P., and Coauthors, 2013: Host model uncertainties in aerosol radiative forcing estimates: Results from the AeroCom prescribed intercomparison study. *Atmos. Chem. Phys.*, **13**, 3245–3270, https://doi.org/10.5194/acp-13-3245-2013.

Swart, N. C., and Coauthors, 2019: The Canadian Earth System Model version 5 (CanESM5.0.3). *Geosci. Model Dev.*, **12**, 4823–4873, https://doi.org/10.5194/gmd-12-4823-2019.

Tsutsui, J., 2020: Diagnosing transient response to CO_2 forcing in coupled atmosphere-ocean model experiments using a climate model emulator. *Geophys. Res. Lett.*, **47**, e2019GL085844, https://doi.org/10.1029/2019GL085844.

Wilcox, L., and Coauthors, 2022: Regional Aerosol Model Intercomparison Project. EGU General Assembly 2022, Vienna, Austria, EGU22-5540, https://doi.org/10.5194/egusphere-egu22-5540.

WMO, 2019: WMO provisional statement on the state of the global climate in 2019. World Meteorological Organization Doc., 35 pp., https://library.wmo.int/index.php?lvl=notice_display&id=21626.

Zanna, L., S. Khatiwala, J. M. Gregory, J. Ison, and P. Heimbach, 2019: Global reconstruction of historical ocean heat storage and transport. *Proc. Natl. Acad. Sci. USA*, **116**, 1126–1131, https://doi.org/10.1073/pnas.1808838115.

Zelinka, M. D., T. A. Myers, D. T. McCoy, S. Po-Chedley, P. M. Caldwell, P. Ceppi, S. A. Klein, and K. E. Taylor, 2020: Causes of higher climate sensitivity in CMIP6 models. *Geophys. Res. Lett.*, **47**, e2019GL085782, https://doi.org/10.1029/2019GL085782.

Zhang, Q., and Coauthors, 2019: Drivers of improved PM2.5 air quality in China from 2013 to 2017. *Proc. Natl. Acad. Sci. USA*, **116**, 24 463–24 469, https://doi.org/10.1073/pnas.1907956116.